

## Airfoil flow separation control with plasma synthetic jets at moderate Reynolds number

Zong, Haohua; van Pelt, Timo; Kotsonis, Marios

**DOI**

[10.1007/s00348-018-2624-y](https://doi.org/10.1007/s00348-018-2624-y)

**Publication date**

2018

**Document Version**

Final published version

**Published in**

Experiments in Fluids

**Citation (APA)**

Zong, H., van Pelt, T., & Kotsonis, M. (2018). Airfoil flow separation control with plasma synthetic jets at moderate Reynolds number. *Experiments in Fluids*, 59(11), Article 169. <https://doi.org/10.1007/s00348-018-2624-y>

**Important note**

To cite this publication, please use the final published version (if applicable).  
Please check the document version above.

**Copyright**

Other than for strictly personal use, it is not permitted to download, forward or distribute the text or part of it, without the consent of the author(s) and/or copyright holder(s), unless the work is under an open content license such as Creative Commons.

**Takedown policy**

Please contact us and provide details if you believe this document breaches copyrights.  
We will remove access to the work immediately and investigate your claim.

# Airfoil flow separation control with plasma synthetic jets at moderate Reynolds number

Haohua Zong<sup>1</sup> · Timo van Pelt<sup>1</sup> · Marios Kotsonis<sup>1</sup>

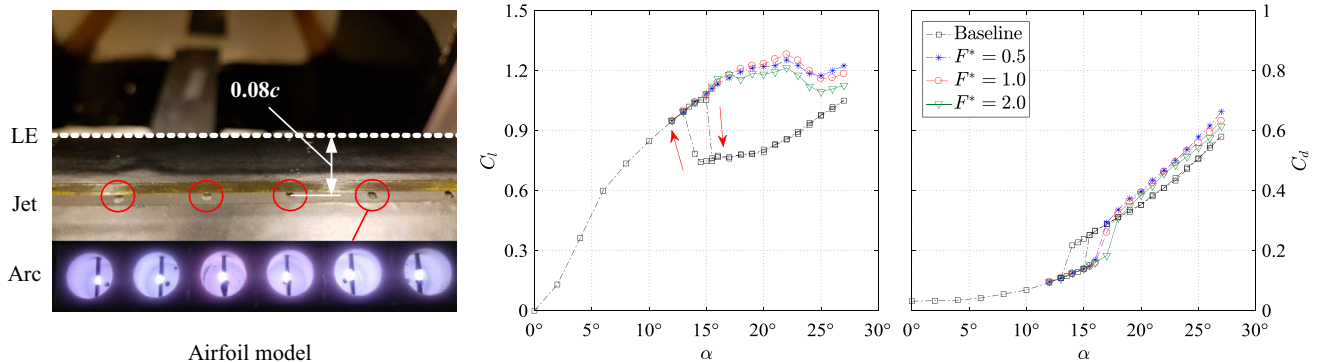
Received: 10 April 2018 / Revised: 17 September 2018 / Accepted: 21 September 2018 / Published online: 15 October 2018  
© The Author(s) 2018

## Abstract

An array of 26 plasma synthetic jet actuators (PSJA) is flush-mounted on a NACA-0015 airfoil model to control the leading-edge flow separation at moderate Reynolds number ( $Re_c = 1.7 \times 10^5$ ). The stall angle of this airfoil is postponed from  $15.5^\circ$  to approximately  $22^\circ$ , and the peak lift coefficient is increased by 21%. PSJAs exhibit distinctive separation control mechanisms depending on the relative location between actuation and separation and reduced frequency of actuation ( $F^*$ ). At an angle of attack of  $\alpha = 15.5^\circ$ , the non-actuated flow separates approximately 4% chord length downstream of the jet orifices. Plasma synthetic jets (PSJs) applied at  $F^* \geq 0.5$  can displace the separation point downstream to mid-chord position, as a result of the energizing of the incoming boundary layer through mixing enhancement. As a comparison, with actuation frequency of  $F^* \leq 0.25$ , the separation point at  $\alpha = 15.5^\circ$  remains near the leading edge and the zero-velocity line is periodically swept towards the suction surface by the convecting spanwise vortices generated from PSJ actuation, leading to a reduction of time-averaged backflow area. For the case of separation control at  $\alpha = 22^\circ$ , the separation point resides always upstream of the actuation position, regardless of actuation frequency. The peak lift coefficient is attained at  $F^* = 1$ , and the decreasing lift at high actuation frequency ( $F^* = 2$ ) is ascribed to the severe interaction between adjacent spanwise vortices at short spacing.

## Graphical abstract

Airfoil flow separation control with plasma synthetic jets at  $Re_c=1.7 \times 10^5$



## 1 Introduction

Flow separation can be found extensively in engineering applications including rotor blades (pitching airfoil), landing gears (cylinder flow), trucks (blunt body flow), inlets of supersonic aircrafts (shock wave/boundary layer interaction, SWBLI) and so on (Simpson 1989). In most occasions, separation is undesired, as extra drag which lowers the vehicle

✉ Haohua Zong  
H.Zong-1@tudelft.nl

<sup>1</sup> Faculty of Aerospace Engineering, Delft University of Technology, Delft, The Netherlands

efficiency and unsteady loads that advance structural fatigue are induced. In an attempt to eliminate airfoil flow separation, both passive (vortex generators, turbulators, etc.) and active approaches are developed (Gad-el Hak et al. 2003). Compared to passive approaches, active flow control, utilizing fluidic and plasma-based actuators are more attractive as no parasitic drag is created during off-operation condition (Cattafesta and Sheplak 2011; Choi et al. 2008).

Fluidic actuators can be mainly distinguished into steady jets, unsteady jets and conventional synthetic jets. In the case of steady jets, the fluid is ejected either tangential to the surface to directly accelerate the near-wall flow, or inclined and skewed (vortex-generator jets) to create streamwise vortices that mix the high-momentum flow in the outer boundary layer with the retarded low-energy flow in the inner layer (Compton and Johnston 1992). Although prominent control effects have been achieved using this technique, the mass flux required by steady blowing is overwhelming. These constrains turn researchers' attention to unsteady jets (Greenblatt and Wygnanski 2000). Pulsing at  $O(0.1\%)$  of the main flow momentum, hydrodynamic instabilities of the separated shear layer are leveraged by unsteady jets to create coherent spanwise vortices. These vortices bring the high-momentum flow from free stream to the near-wall region, thus reattaching/deflecting the separated shear layer in a proper frequency range ( $0.3 \leq F^+ \leq 4$ ,  $F^+$  is the reduced frequency normalized by free stream velocity and separation length) (Seifert et al. 2004). Conventional synthetic jets refer to zero-net mass flow jets produced by oscillating membranes or pistons. In low-frequency range ( $F^+ \sim O(1)$ ) (Glezer et al. 2005), conventional synthetic jets actuate the separated flow similarly to unsteady jets. Nevertheless, at high actuation frequency ( $F^+ \sim O(10)$ ), the so-called virtual aeroshaping effect of synthetic jets becomes the dominant control mechanism. Specifically, a localized mean recirculation zone is formed near the jet orifice, superimposing a virtual hump on the geometric airfoil profile (Mittal and Rampungoon 2002). This virtual hump alters the streamwise pressure gradient, leading to complete or partial suppression of the separation (Glezer et al. 2005).

Compared to fluidic actuators, plasma actuators, including surface dielectric barrier discharge actuators (SDBDAs) and plasma synthetic jet actuators (PSJAs), show attractive features such as simple construction, fast response and high bandwidth (Corke et al. 2010). Typical configurations of SDBDAs are a pair of electrode strips isolated by dielectric layers. The anode strip is either supplied with high-voltage sinusoidal signals ( $O(10 \text{ kHz})$ ) that impose plasma-induced body forces on the near-wall boundary layer, or nanosecond high-voltage pulses that release thermal perturbations ( $\approx 700 \text{ K}$ ) (Roupassov et al. 2009; Correale et al. 2014). As the body force created by sinusoidal driven signals is confined to the order of  $O(10 \text{ mN/m})$  for single SDBDA (Benard

and Moreau 2014), successful separation control using this momentum-addition method (similar to tangential wall-jets) has been demonstrated only up to  $U_\infty \leq 30 \text{ m/s}$  (Post and Corke 2004a). SDBDAs driven by nanosecond pulses have been demonstrated to control the flow separation in a Mach range of 0.05–0.85 (Roupassov et al. 2009). Based on Little et al. (2012), this device controls the separation by either acting as an active trip at pre-stall angles of attack, or utilizing shear-layer stability to produce coherent large-scale vortices at post-stall conditions, similar to unsteady jets. Nevertheless, for the case when shear-layer stability is absent and natural transition has already ensued (e.g., trailing edge separation at high-Reynolds number), SDBDAs driven by nanosecond pulses effectively lose their control authority.

Plasma synthetic jet actuators (PSJA), also named as sparkjet actuators, were proposed by Grossman et al. (2003) for high-speed high-Reynolds-number flow control. Utilizing rapid spark discharge to pressurize air in an enclosed cavity, high-velocity pulsed jets (300 m/s) as well as intense shock waves can be generated reliably at a repetition rate of up to 5 kHz (Narayanaswamy et al. 2010). So far, PSJAs are mainly used to reduce the mean separation region (Greene et al. 2015) as well as the low-frequency unsteadiness induced by SWBLI (Narayanaswamy et al. 2012). The current work deals with the application of PSJA in airfoil flow separation control at high-Reynolds number. Compared to other plasma actuators, PSJAs have the potential to control several types of flow separation by leveraging both momentum and instability mechanisms. Specifically, for turbulent trailing-edge separation, PSJAs can act as vortex generators, creating streamwise vortices to enhance the mixing and suppress the separation (Caruana et al. 2013). Alternatively in the case of leading-edge separation where hydrodynamic instabilities are present, the thermal/momentum perturbations generated by PSJAs are expected to be analogous to the mechanism employed by nanosecond SDBDAs.

In Caruana et al. (2013), the feasibility of PSJAs in trailing edge separation control was demonstrated experimentally. 20 PSJAs were embedded  $0.32c$  ( $c$  is the chord length) downstream of the leading edge to eliminate the limited trailing edge separation over a NACA-0015 airfoil. At a freestream velocity of 20 m/s ( $Re_c = 6.7 \times 10^5$ ), a drag reduction of up to 13% was reported by examining the wake velocity profile. In contrast, results on leading-edge control with PSJAs have not been reported yet. The present work fills this gap and validates the control authority of PSJAs in leading edge separation at a chord-based Reynolds number of  $Re_c = 1.7 \times 10^5$ . This Reynolds number is lower from what is typically encountered in commercial aircrafts/ transportation trucks ( $O(10^6 - 10^7)$ ), yet still relevant to small-scale unmanned vehicles and low-speed vertical axis wind tunnels (Timmer 2008). 26 PSJAs are embedded in a NACA-0015 airfoil ( $\alpha$ ) and fed by a novel sequential

discharge power supply. The overall change of the lift and drag coefficients are measured by a balance system, while the control mechanisms at various actuation frequencies are exploited with a high-speed Particle Imaging Velocimetry (PIV) system. Details on the experimental setup are introduced in Sect. 2. Force measurement results and PIV results are presented in Sects. 3 and 4.

## 2 Experimental setup

### 2.1 Wind tunnel, airfoil model and actuators

A NACA-0015 airfoil was 3D printed in polyamide and used in this study, as shown in Fig. 1b. The chord length ( $c$ ) and span are 250 mm and 400 mm, respectively. Near the leading edge, a rectangular groove extending the whole span (height 10 mm, depth 13 mm) is milled to accommodate the actuators. (Amitay et al. 2001) demonstrated that the optimal actuation position for synthetic jets-based separation control should be just upstream of the separation point. In this study, the separation point at stall angle of attack ( $15.5^\circ$ ) is located at approximately  $0.12c$  downstream of the leading edge. To avoid the high wall shear stress created by synthetic jets in cross flow, damped out during downstream convection, the distance between separation point and jet exit should be limited to 5–7 times of the exit orifice diameter (i.e., 3–5% chord length) (Zong and Kotsonis 2017b;

Lardeau and Leschziner 2011). As such, the chordwise distance between the actuator exit orifice center and the leading edge is designed to be 20 mm ( $0.08c$ ). A spacious chamber (width 58 mm, height 16 mm) is created inside the airfoil model to accommodate the capacitors and resistors necessary for the realisation of multi-channel arc discharge (see Sect. 2.2). As a result, only two thin soft wires are connected to power the actuators, largely mitigating the interference of stiff cable connections on force balance measurements.

This model is tested in the W-tunnel of Delft University of Technology. The W-tunnel is an open-jet subsonic wind tunnel with interchangeable contraction segments. A wooden contraction segment with a square  $400 \times 400 \text{ mm}^2$  exit is used in this study, and the freestream turbulence level is typically less than 0.5% at the maximum achievable velocity of 35 m/s. As shown in Fig. 1a, the contraction part is followed by a rectangular plexiglass test section (length 600 mm) which enables optical measurements. The airfoil model is mounted between the two side walls of the plexiglass test section, and the pivot point is located at  $0.25c$  away from the leading edge.

Multiple plasma synthetic jet actuators are arranged in one row to cover the entire span of the airfoil. As shown in Fig. 1b, the actuator array is mainly constructed out of a ceramic bar (material MACOR, cross section  $10 \text{ mm} \times 10 \text{ mm}$ ) where multiple cylindrical cavities are machined, and a flat ceramic cap (thickness 3 mm) with uniformly distributed orifices in the spanwise direction

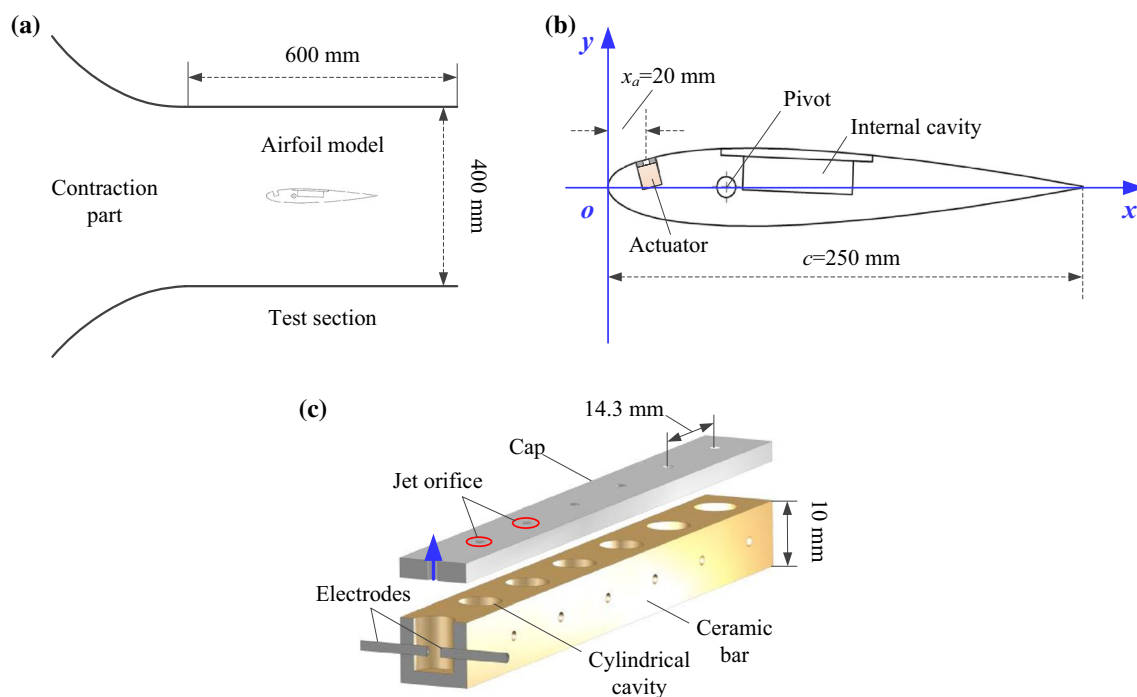


**Fig. 1** Sketches of **a** model placement in test section (to scale), **b** airfoil model and **c** actuator array

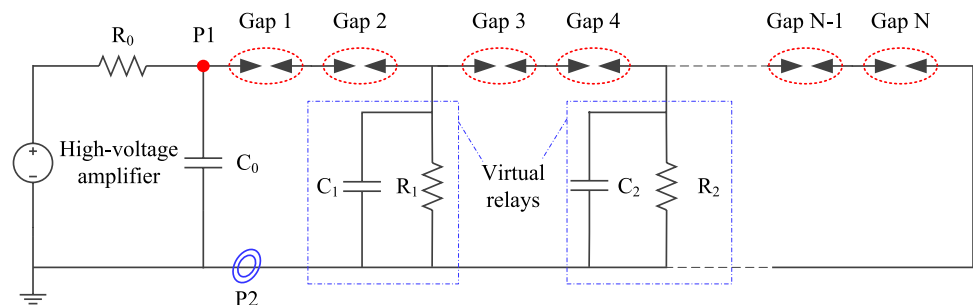
( $z$ -direction). After assembly of the airfoil model and the actuator components, the discontinuity of airfoil profile incurred by the flat ceramic cap is subsequently diminished by a thin smooth dark tape wrapped around the model (thickness 0.1 mm), which also eliminates the laser reflection and guarantees a natural flow transition. The remaining disturbance is comparable to that created by the exposed electrodes of typical SDBDAs in similar flow control applications (Corke et al. 2010). The inner diameter and height of the cylindrical cavities are 6 mm and 8 mm, respectively, resulting in a cavity volume of 226 mm<sup>3</sup>. For each cavity, two electrodes are inserted from opposite directions, acting as anode and cathode, respectively. The inter-electrode gaps are set uniformly as 2 mm for all the actuators except for the first two for trigger purposes as will be explained later on. The axes of the cavities and the circular orifices in the cap are aligned to create pulsed jets that are normal to the local airfoil surface (i.e., ‘vertical’ jets), as Postl et al. (2011) have shown that the pulsed ‘vertical’ injection outperforms the pulsed angled injection in separation control. Determination of the spanwise spacing of actuators is mainly driven by the amount of actuators that can be fed in a stable manner by the used power supply as well as the necessary high-voltage insulation between connection cables. Theoretically, the amount of actuators should be maximized to get a higher jet momentum coefficient favouring the flow separation control. Practically, as more and more actuators are coupled in the discharge circuit, the possibility of trigger failure increases significantly; meanwhile, unexpected sparks occur frequently between the connecting cables due to short spacing. Constrained by these factors, a maximum of 26 actuators are accommodated in the specially arranged groove in the airfoil model, corresponding to a spanwise spacing of 14.3 mm. In Zong and Kotsonis (2017b), the maximum spanwise affected extent of PSJs is demonstrated to be approximately 10 times of the orifice diameter. As such, the jet orifice diameter is designed roughly as one tenth of the actuator spacing, i.e., 1.5 mm, to integrate ‘seamlessly’ the spanwise influence of adjacent PSJs.

## 2.2 Discharge scheme and power supply system

The discharge circuits proposed by Zhang et al. (2017a) and Zong and Kotsonis (2017c) are combined to power the actuator array in this study. Figure 2 shows the power supply system. A high-voltage amplifier (Trek model, 20–20HS), a current-limiting resistor  $R_0$  (resistance 500 k $\Omega$ , power 200 W) and an energy-storing capacitor  $C_0$  (capacitance 4 nF, withstanding voltage > 20 kV) constitute the charge circuit. All the gaps are connected in series with the energy-storing capacitor. One virtual relay is added between every two actuators and the ground to enable the sequential breakdown of these gaps (Zhang et al. 2017b). The virtual relay, namely a parallel connection of a small capacitor (capacitance 0.1 nF) and a large resistor (resistance 2 M $\Omega$ , power 6 W), is designed to match the dynamic impedance of the pulsed arcs. Depending on whether all the gaps have been ignited, the working process of this power supply system can be split into two phases, pre-trigger discharge phase and capacitive discharge phase.

The detailed workflow is as follows. In the pre-trigger discharge phase, high-voltage pulses (voltage 20 kV, pulse width 3 ms) are delivered by the amplifier to the charge capacitor  $C_0$ . As all the capacitors ( $C_1, C_2 \dots$ ) are vacant (zero initial voltage) prior to discharge ignition, the virtual relays can be treated as short circuits at this stage. Thus, the increasing voltage across  $C_0$  is carried solely by Gap 1 and Gap 2. For two gaps with 2 mm spacing, the breakdown voltage (denoted as  $U_b$ ) is approximately 9 kV (Zong and Kotsonis 2017c). After the ignition of Gap 1 and Gap 2, the capacitor in the first virtual relay ( $C_1$ ) is charged by  $C_0$  in less than 1  $\mu$ s, and the high voltage across  $C_1$  is further transferred to Gap 3 and Gap 4. Consequently, Gap 3 and Gap 4 are ignited. This sequence repeats until the complete junction of all the gaps. Note that there is no virtual relay between the last actuator and the ground. During this pre-trigger process, the arc is relatively weak in intensity (energy level  $C_1 U_b^2/2$ ) and mainly sustained by the leakage current running through the resistors ( $R_1, R_2, \dots$ ). After the complete junction of the gaps, the energy stored in all the capacitors is released simultaneously through the multi-arc channel, creating an intense capacitive discharge (energy level

**Fig. 2** Power supply system. The actuators are modeled as the gaps. P1 and P2 indicate the measurement stations of the discharge voltage and the current, respectively





$C_0 U_b^2/2$ ) that is responsible for heating and pressurising the cavity gas. The working frequency of this actuator array can be tuned directly by the discharge frequency. Limited by the output power of the high-voltage amplifier, the maximum reliable discharge frequency is approximately 100 Hz.

The discharge current ( $I_d$ ) and the discharge voltage ( $U_d$ ) are measured by a high-voltage probe (Tektronix, P6015a) and a current monitor (Pearson, Model 325), respectively, at the stations indicated in Fig. 2. The measured signals are recorded by an digital oscilloscope (Tektronix, TDS3054C) at a sampling rate of 1 GHz. Representative voltage and current waveforms are shown in Fig. 3. Note that the first two electrode gaps are enlarged to 3 mm to create an overshoot breakdown voltage (14 kV) for the subsequent gaps (spacing 2 mm) so that the energy dissipated in the pre-trigger discharge phase can be compensated (Zhang et al. 2017b). The pre-trigger discharge sustains approximately 0.8  $\mu$ s and characterised by a staggered declination of the discharge voltage and a relatively low discharge current ( $O(10$  A)). In the capacitive discharge phase, both the discharge voltage and the discharge current oscillate periodically with damping amplitudes. This is largely expected, as the capacitors, arc channels and the parasitic wire inductance constitute a typical RLC oscillation circuit (Belinger et al. 2014). The peak current at this phase reaches about 300 A and the duration is approximately 2  $\mu$ s. The total discharge energy ( $E_d$ ) integrated from the voltage and the current waveforms is approximately 0.42 J, and a vast majority is deposited in the capacitive discharge phase.

### 2.3 Baseline actuator characteristics

Extensive characterization studies of plasma synthetic jets operating in quiescent air have been performed by Zong and

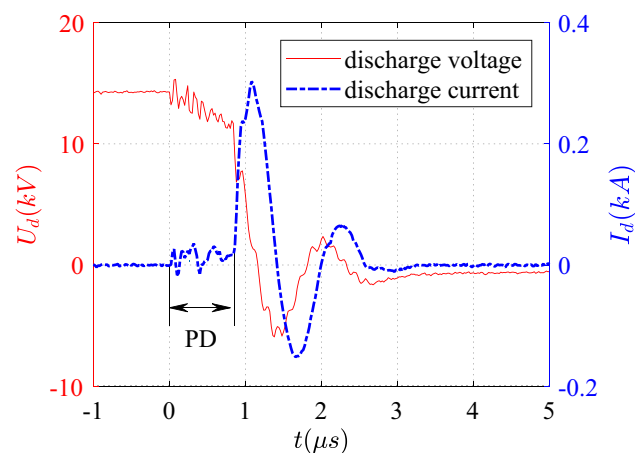


**Fig. 3** Representative voltage and current waveforms. PD indicates the pre-trigger discharge

Kotsonis (2016a, b, 2018), using phase-locked PIV measurements. As the geometric configurations of the present actuator (i.e., two electrodes plus a cylindrical cavity) and power supply (i.e., capacitive discharge circuit) bear significant similarities with those adopted in the previous studies, the general characteristics of the presently used plasma synthetic jet are expected to remain similar and can be captured relatively well by theoretical analysis.

Analytical models developed by Haack et al. (2010) and Anderson and Knight (2012) show that the peak jet velocity ( $U_p$ ) and mean jet momentum ( $M_e$ ) are mainly determined by the nondimensional energy deposition ( $\epsilon$ , defined as the ratio of arc discharge energy to the initial internal energy of the cavity gas) (Zong and Kotsonis 2018), and the gas heating efficiency ( $\eta_h$ ) which can be influenced significantly by the electrode configuration and atmospheric parameters. Based on the measured discharge energy ( $E_d$ ) and the geometrical parameters of actuator cavity in this study (cavity volume, electrode distance, etc.),  $\epsilon$  and  $\eta_h$  are estimated to be 0.28 and 10%, respectively (Smy et al. 1983; Zong et al. 2016). Using these parameters as the input, the peak jet velocity can be computed with the following analytical relations (Haack et al. 2010; Anderson and Knight 2012; Zong et al. 2015),

$$\begin{cases} T_{ca}/T_0 = 1 + \eta_h \epsilon \\ P_{ca} = \rho_0 R T_{ca} \\ P_{ca}/P_0 = \left(1 + \frac{\gamma - 1}{2} M_p^2\right)^{\gamma/(\gamma - 1)} \\ T_{jet}/T_{ca} = (P_0/P_{ca})^{(\gamma - 1)/\gamma} \\ U_p = M_p \times \sqrt{\gamma R T_{jet}}, \end{cases} \quad (1)$$

where  $R$  and  $\gamma$  are the gas constant and the specific heat ratio of air, respectively;  $P_0$  and  $\rho_0$  denote the ambient temperature and density;  $T_{ca}$  and  $P_{ca}$  represent the peak temperature and pressure of the actuator cavity reached after energy deposition;  $M_p$  and  $U_p$  are the peak exit Mach number and the peak exit velocity in jet stage. These relations are derived under the assumptions that energy deposition stage and jet stage can be treated respectively as a constant volume heating process and an isentropic expansion process (Zong et al. 2015). As a result,  $U_p$  is computed to be 68 m/s ( $M_p = 0.2$ ), resulting in a peak jet-to-crossflow ratio of 6.8. Additionally, Zong and Kotsonis (2017a, 2018) have demonstrated that the duration of primary jet stage ( $T_{jet}$ , jet duration time) is close to the natural Helmholtz oscillation period of the actuator cavity, which is computed to be 362  $\mu$ s based on the throat length, cavity volume and exit orifice diameter (Zong and Kotsonis 2017a, 2018; Chiatto and de Luca 2017).

In Anderson and Knight (2012), the nondimensional impulse pertaining to single jet pulse ( $I_p^*$ ) is derived as a function of the dimensionless energy deposition [Equation

(36) in their study]. With this relation, the jet–crossflow momentum ratio ( $C_\mu$ , i.e., blowing momentum coefficient) can be estimated as follows (Seifert et al. 2004),

$$C_\mu = \frac{f_d \times I_p^* \sqrt{\rho_0 V_{ca} E_d \eta_h}}{\rho_0 U_\infty^2 \times c s_a}, \quad (2)$$

where  $s_a$  is the actuator spacing in spanwise direction (14.3 mm, see Fig. 1). As evidenced, the blowing momentum coefficient increases linearly with the discharge frequency. For the peak value of  $f_d = 80$  Hz used in this investigation,  $C_\mu$  is computed to be  $4.5 \times 10^{-5}$ , which falls into the typical range of oscillatory jets and conventional synthetic jets, i.e.,  $O(0.001\text{--}0.1\%)$  (Seifert et al. 2004; Amitay et al. 2001).

## 2.4 Measurement scheme

A six-component load-cell balance system developed by NLR (National Aerospace Laboratory, the Netherlands) is used to measure the overall aerodynamic forces and moments imposed on the airfoil model. At each angle of attack, the balance signals are acquired for 3 s at a sampling rate of 2 kHz. Low-pass filtering and ensemble averaging are applied on the recorded signals later on to reduce the measurement uncertainty. The errors for lift and drag measurement are estimated to be less than 5 mN (0.1% of peak lift) and 10 mN (0.3% of peak drag), respectively. Wind tunnel blockage corrections are applied on the computed lift and drag coefficient using the methods proposed in Maskell (1963).

The mid-span velocity field above the suction side of the airfoil is measured by a high-speed planar PIV system which consists of a high-speed camera (Photron Fastcam SA-1, resolution  $1024 \times 1024$  pixels), a high-speed laser (Quantronix, Darwin Duo 527-80-M) and a programmable timing unit (LaVison, high-speed PTU). The laser beams emitted from the laser head are shaped into a laser sheet (thickness 1 mm) by a combination of two spherical lenses and one cylindrical lens. This laser sheet passing through the mid-span plane is kept strictly normal to the airfoil surface. Liquid particles are produced by a SAFEX fog generator in the settling chamber of the wind tunnel using water–glycol mixture as the working fluid. The mean particle diameter is approximately 1  $\mu\text{m}$ , and the particle image size is kept to approximately 2 pixels. The camera is mounted with an objective of 105 mm (Nikon, Micro Nikkor) to image a field of view (FOV) of  $270 \text{ mm} \times 270 \text{ mm}$ , leading to a magnification ratio of 0.075. LaVision Davis 8.3.1 is used for recording and processing the raw particle images pairs. The interrogation window size and the overlapping ratio in the final pass are set as  $32 \times 32$  and 75%, respectively, resulting in a final spatial resolution of 2.1 mm/vector.

In this study, the nominal free stream velocity ( $U_\infty$ ) is kept constant at 10 m/s, corresponding to a chord-based Reynolds number ( $Re_c$ ) of  $1.7 \times 10^5$  (ambient temperature 293 K, ambient pressure 1.01 bar). The dimensionless actuation frequency (namely Strouhal number) is defined as  $F^* = f_d c / U_\infty$ , where  $f_d$  denotes the discharge frequency. Similarly, time is normalized by  $c / U_\infty$ , resulting in a dimensionless convection time,  $T^* = t U_\infty / c$ . In Seifert et al. (2004), the distance between separation point and trailing edge (i.e., separation length,  $L_s$ ) is selected as the reference length scale, resulting in another dimensionless frequency  $F^+ = f_d L_s / U_\infty$ . For the current investigation, leading-edge separation is dominant, and  $L_s$  varies only marginally around  $0.9c$  at the two investigated angles of attack ( $\alpha = 15.5^\circ, 22^\circ$ ). As such, negligible differences will be introduced by the distinct usage of the dimensionless frequency, and  $F^*$  is used to display the results throughout this paper.

A wide range of  $0.1 \leq F^* \leq 2$  is tested with plasma actuation. PIV measurements are performed at several representative angles of attack where flow separation is expected. For each of the tested cases, a long sequence containing 2400 image pairs is acquired at a sampling rate of 800 Hz, which is 40 times higher than the vortex shedding frequency reported by Yarusevych et al. (2009) (reference value  $0.5 U_\infty / c$ ) and sufficient to get relevant frequency spectrums. Both balance and PIV measurements are synchronised with the discharge ignition to facilitate the computation of phase-averaged results. Peak detection error and finite ensemble size are identified as the two main sources of velocity measurement uncertainty in this study. The maximum particle displacement is kept as 10 pixels. Considering a typical peak detection error of 0.2 pixels in cross-correlation maps, a relative uncertainty of 2% is expected on the instantaneous velocity field. For ensemble-averaged velocity fields, the uncertainty caused by finite sample size can be computed from the the root mean square of velocity fluctuations (Sciacchitano and Wieneke 2016). As a result, the total uncertainty in time-averaged and phase-averaged velocity fields is estimated to be less than 1% and 5% of  $U_\infty$ , respectively.

## 3 Balance measurement results

Square-wave tests are first preformed to determine the time-scales needed by the flow to respond to plasma actuation. During these tests, PSJAs are switched on and off alternately (cycle period 5 s, duty cycle 50%), and the instantaneous lift and drag traces obtained from multiple repetitive measurements are phase-averaged. Figure 4 shows the phase-averaged traces of the lift and drag coefficients (denoted as  $C_l$  and  $C_d$ ) measured at  $F^* = 1$  and  $\alpha = 15.5^\circ$  (stall angle). After plasma actuation is switched on, it takes approximately

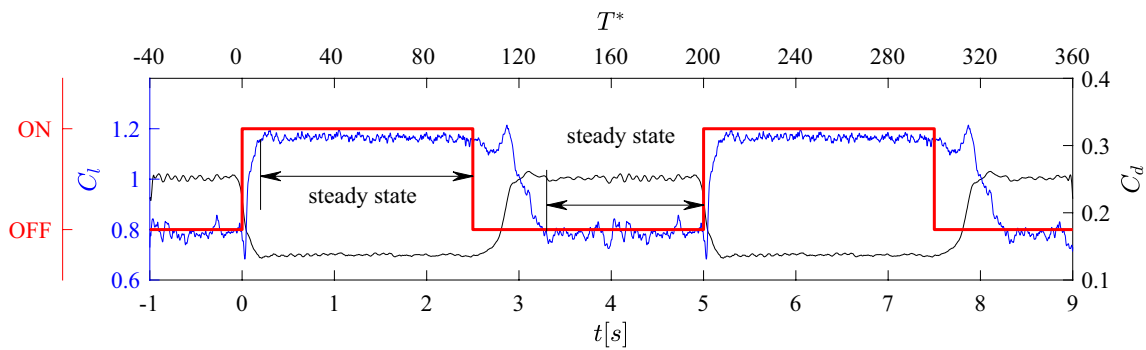


**Fig. 4** Phase-averaged variations of the lift and drag coefficients ( $C_l$ ,  $C_d$ ) at  $\alpha = 15.5^\circ$  during a square wave test. ‘ON’ and ‘OFF’ indicate the status of the plasma actuation. The dimensionless discharge frequency at ‘ON’ status is  $F^* = 1$

2–3 dimensionless time units for the forces to reach a steady state. Comparing the steady-state values to the baseline ones, a considerable augmentation/reduction in lift/drag is observed. Once the actuation is seized, these forces start to resume, experiencing a considerably longer transient process (30 time units). During this process, the high-lift low-drag status is sustained for roughly 15 dimensionless time units before a mild recovery to the original status begins. The distinct timescales for separation and reattachment to occur were carefully interpreted by Benard et al. (2011). For the forced attachment case, the spanwise vortices created by plasma actuation propagate rapidly downstream at a velocity of  $0.43U_\infty$ , leading to a rapid transition of the separation point from leading edge to trailing edge. As a comparison, during the natural separation process, the growth of localised trailing-edge separation to massive leading-edge separation is much slower, ostensibly due to the low backflow velocity (typically less than  $0.2U_\infty$ ). This hysteresis effect is further

utilized by Benard et al. (2011) to create a real-time feedback control system which operates DBD actuators in low duty cycle to minimize the power consumption.

The lift and drag coefficients at increasing angles of attack for both baseline and actuated cases are shown in Fig. 5. Without PSJ actuation, the airfoil stalls at  $\alpha = 15.5^\circ$ , signified by an abrupt change of the lift and drag coefficients. A hysteresis loop is exhibited between  $\alpha = 13^\circ$  and  $\alpha = 15^\circ$ , which is expected for this type of airfoil at a chord-based Reynolds number of  $O(10^5)$  (Marchman et al. 1987; Timmer 2008). When PSJ actuation is applied, the stall angle is postponed to approximately  $22^\circ$ , and the hysteresis loop observed in the baseline case is completely eliminated, which is consistent with the observations of Post and Corke (2004b) where the same airfoil (NACA-0015) is tested with SDBDAs at  $Re_c = 1.6 \times 10^5$ . These results indicate that PSJAs can be potentially applied to increase the blade loads of vertical-axis wind turbines

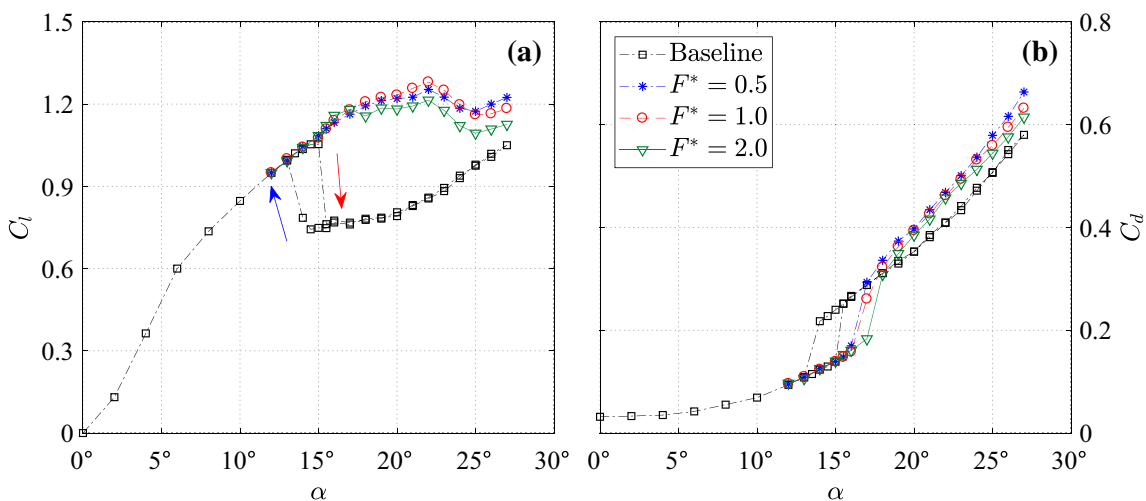


**Fig. 5** **a** Lift and **b** drag coefficients for both baseline and actuated cases. The hysteresis loop is indicated by a red arrow for increasing  $\alpha$  and blue arrow for decreasing  $\alpha$



(Timmer 2008), or to mitigate the unsteady force of pitching airfoils, where the structure fatigue is tightly associated with the hysteresis loops (Corke and Thomas 2015). It should be noticed that the boundary layer status at separation point is left undetermined in this investigation; thus, the above-mentioned flow phenomenon could be altered when the chord-based Reynolds number changes. In terms of peak lift augmentation ( $\alpha = 22^\circ$ ),  $F^* = 1$  outperforms the other two cases and the peak lift coefficient is increased by 21%. For the drag coefficient shown in Fig. 5b, each curve consists of two segments. The first segment ( $\alpha < 13^\circ$ ) roughly follows a quadric relation corresponding to the induced and parasitic drags of attached flow, while the second segment ( $\alpha > 13^\circ$ ) is resulting from the high pressure drag under stall conditions. In the range of  $0.5 \leq F^* \leq 2.0$ , higher actuation frequency can prolong the first segment of the drag curves to higher angle of attack ( $16.5^\circ$  at  $F^* = 2.0$ ), while slightly increasing the drag in the second segment.

A metric quantifying the effectiveness of actuators (power saving ratio, denoted as  $\eta$ ) can be defined as shown in Eq. (3).  $\Delta D$  represents the variation in drag force.  $\eta$  is essentially the ratio of the power saved from drag reduction to the power needed to feed the actuators. At  $\alpha = 15.5^\circ$  and  $F^* = 0.5$ , the power saving ratio is estimated to be 0.74; thus, further efforts should be made to elevate the efficiency of PSJA array for industrial applications. In Jukes and Choi (2009), the denominator of Eq. (3) is replaced by the fluidic power generated by plasma, and the power saving ratio of DBD actuators in cylinder flow control is estimated to be 1500. This ostensibly astonishing distinction (almost 2000 times) can be well explained by the electro-mechanical efficiency of plasma actuators, which is defined as the ratio of the fluidic power outputted to the electrical power ingested. Giepmans and Kotsonis (2011) has reported that the electro-mechanical efficiency of SDBDAs is  $O(0.1\%)$ . Taking this value into account, the power saving ratios of PSJAs and DBDAs fall in the same order,  $\eta \sim O(1)$ .

$$\eta = \frac{\Delta D \times U_\infty}{f_d \times \int_0^{T_d} U_d(t) I_d(t) \times dt} \quad (3)$$

## 4 PIV results and analysis

This part is organised as follows. An overview of the baseline flow scenarios is provided in Sect. 4.1, according to which two cases ( $\alpha = 15.5^\circ$ , and  $22^\circ$ ) are picked out to perform detailed PIV measurements. Subsequently, the control effects as well as the control mechanisms in these two cases are presented in Sects. 4.2 and 4.3.

### 4.1 Time-averaged velocity fields for baseline case

The time-averaged velocity fields at increasing angle of attack are shown in Fig. 6 for the baseline case (i.e., no actuation). At  $\alpha = 13^\circ$ , a small region of separated flow is observed near the trailing edge, as bounded by the dividing streamline. It must be noted here that the dividing streamline is defined as the flow streamline originating at the separation point, and not to be confused with the zero-velocity line. The near-wall flow in this separation region is directed upstream by the adverse pressure gradient, producing a prominent backflow region underneath the zero-velocity line ( $U_x = 0$  m/s). This zero-velocity line, serving as the interface between forward and backward flow, defines the time-averaged location of the separated shear layer. With increasing angle of attack from  $\alpha = 13^\circ$  to  $\alpha = 15^\circ$ , the separation region extends upstream. The airfoil stalls at  $15.5^\circ$ , indicated by a jump of the separation point from mid-chord to the vicinity of the leading edge. This causes a sudden drop of the lift and a considerable increase of the drag as shown in Fig. 5. Based on the observed changes and regimes in separation location and separation type (Maskell 1963), two angles of attack ( $\alpha = 15.5^\circ$  and  $22^\circ$ ) are selected to execute detailed PIV measurements, where the separation point lies respectively  $4\%c$  downstream and  $1\%c$  upstream of the jet orifices. These two angles represent the stall angles at baseline and actuation conditions. In both cases, a wide range of  $0.1 \leq F^* \leq 2$  is tested to elucidate the pertinent frequency effects.

### 4.2 Leading edge separation control at $\alpha = 15.5^\circ$ (actuation upstream of separation)

The first examined case pertains to the stall angle ( $15.5^\circ$ ). Figure 7 shows the time-averaged velocity fields at  $\alpha = 15.5^\circ$  with PSJ actuation. In the range of  $0.25 \leq F^* \leq 2.0$ , all the cases exhibit noticeable reduction of the backflow area ( $A_b$ , defined as the area enclosed by the dividing streamline, airfoil model and a vertical line passing through the trailing edge). At  $F^* = 0.25$ , the separation point remains near the leading edge, whereas the dividing streamline bends towards the suction surface compared to the baseline in Fig. 6c, reducing the separation region into a narrow band. For cases of  $F^* \geq 0.5$  (Fig. 7b–d), a much fuller velocity profile is observed near the leading edge, and the flow remains attached during the first half chord. Large-scale leading edge separation is converted into localised trailing edge separation, similar to the base flow scenario exhibited at  $\alpha = 15^\circ$ . To quantify the frequency effect, the dimensionless backflow area ( $A_b^*$ ) and separation length ( $L_s^*$ ) are defined,

$$\begin{cases} A_b^* = \frac{A_b}{0.5c^2 \times \sin(\alpha) \cos(\alpha)} \\ L_s^* = 1 - \frac{x_s}{c \times \cos(\alpha)}, \end{cases} \quad (4)$$

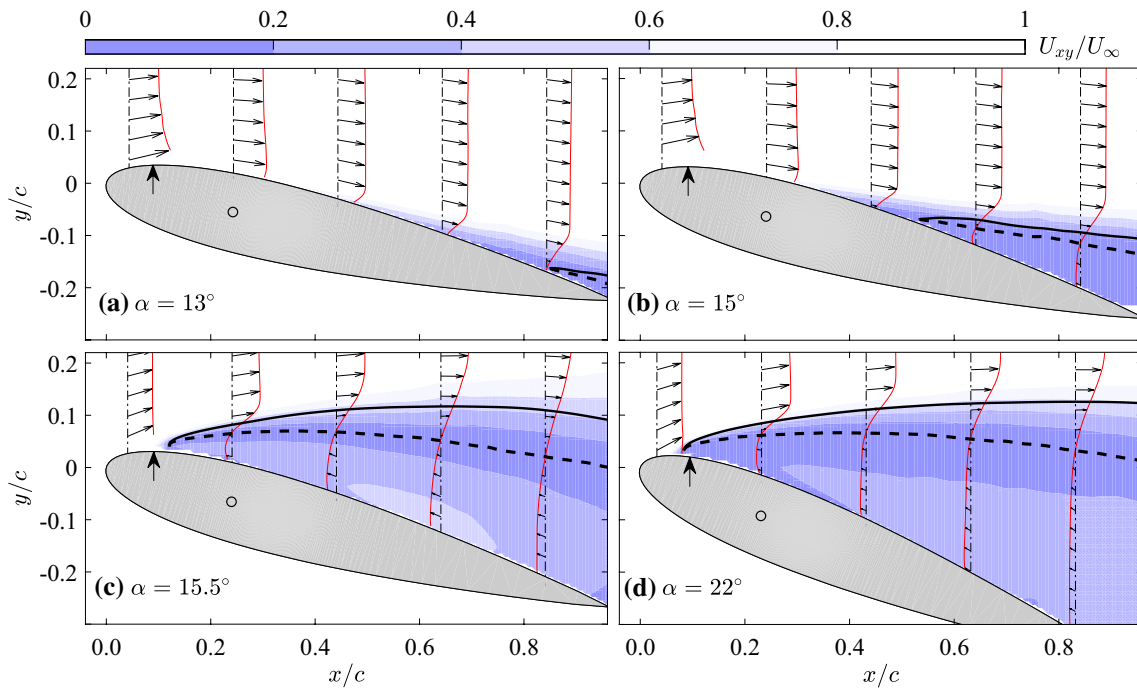


**Fig. 6** Time-averaged velocity fields without plasma actuation (baseline case); the Euclidean sums of the in-plane velocity (denoted as  $U_{xy}$ ) are shown as contours. The velocity profiles at selected chordwise locations are indicated by thin black arrows and red lines. The

black solid lines are dividing streamlines, while the dashed black lines are contour lines of  $U_x = 0$  m/s (termed as zero-velocity lines hereinafter). The jet orifice location is pinpointed by a thick black arrow

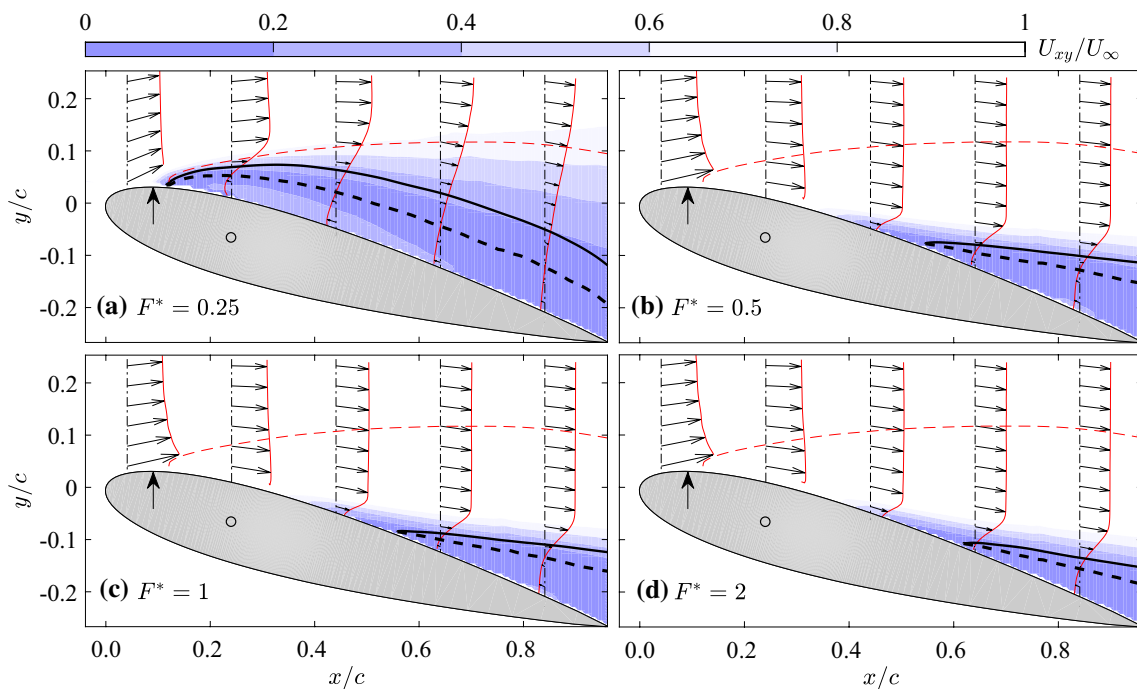


**Fig. 7** Time-averaged velocity fields at  $\alpha = 15.5^\circ$  with PSJ actuation. The plotting methods are identical to the ones used in Fig. 6. The thin red dashed line indicates the zero-velocity line corresponding to the baseline condition

where  $x_s$  denotes the  $x$ -coordinate of the separation point; the triangular area formed by chord and its projections in two axes, namely  $0.5c^2 \times \sin(\alpha)\cos(\alpha)$ , is used to normalize  $A_b$ .

Variation of the dimensionless backflow area, separation length and lift coefficient with actuation frequency at  $\alpha = 15.5^\circ$  is shown in Fig. 8a. Under baseline condition,  $A_b^*$  is close to 1. With increasing frequency, the dimensionless backflow area decreases monotonically and reaches approximately 0.14 at  $F^* = 2$ . Note that a kink point exists at  $F^* = 0.5$  after which the decrease of  $A_b$  is marginal. The separation length remains approximately unchanged ( $0.88c$ ) before this kink point, drops sharply between  $F^* = 0.25$  and  $F^* = 0.5$ , and changes mildly afterwards. Additionally, the lift coefficient increases with decreasing backflow area as expected. These observations lead to a reduced frequency range of  $F^* \geq 0.5$  for favourable leading-edge separation control, which agrees with the review in Seifert et al. (2004).

Flow separation is closely related to the velocity profiles in the boundary layer. A widely used metric to quantify the fullness of velocity profiles is the shape factor, which is defined as the ratio of momentum thickness to displacement thickness ( $H = \delta^*/\theta$ ) as shown in Eq. (5) (Schlichting and Gersten 2017).  $U_s$  denotes the wall-parallel velocity component in the boundary layer. These integrals are computed along the wall-normal direction, starting from the suction surface ( $y_w$ ) and ending at the position where the peak value of wall-parallel velocity ( $U_{s,max}$ ) is attained ( $y_{ref}$ ).

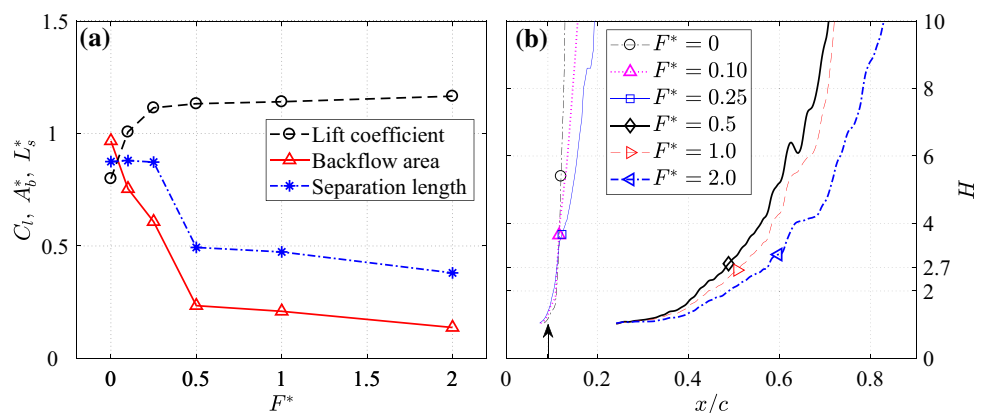
$$\begin{cases} \delta^* = \int_{y_w}^{y_{ref}} \left(1 - \frac{U_s}{U_{s,max}}\right) dy \\ \theta = \int_{y_w}^{y_{ref}} \frac{U_s}{U_{s,max}} \left(1 - \frac{U_s}{U_{s,max}}\right) dy \end{cases} \quad (5)$$

Chordwise variations of boundary layer shape factor for increasing frequency are shown in Fig. 8b. Note that boundary layer transition near the leading edge is not determined from the current PIV measurements due to a large vector

pitch (2.1 mm). For all cases, the shape factor grows monotonically in the chordwise direction. Under low-frequency actuation of  $F^* \leq 0.25$ , the growth rate of  $H$  is slightly postponed by plasma actuation, whereas at high-frequency actuation of  $F^* \leq 0.5$ , the boundary layer shape factors are suppressed below 2 until  $x = 0.2c$ . Simpson (1989) suggested a criterion of  $H = 2.7$  for turbulent flow detachment. The separation point determined by this criterion (not shown) is consistent with that obtained from the zero-velocity line in Fig. 8a. According to the boundary layer equations (Schlichting and Gersten 2017), evolution of the boundary layer velocity profile is affected by both the Reynolds stresses and the streamwise pressure gradient. The low boundary layer shape factor in the actuated cases suggests a fuller velocity profile, and thus higher mixing rate in boundary layers, which can be attributed to the earlier transition or the counter-rotating vortex pairs generated by PSJs (Zong and Kotsonis 2017b). Further studies are necessary to identify which mechanism plays a dominant role in mixing enhancement, under PSJ actuation.

Figure 9 displays the velocity fluctuations ( $U_{rms}$ ) in three representative cases.  $U_{rms}$  is computed as the Euclidean sum of the root mean square (RMS) of in-plane velocity components. High RMS values are always observed in the separation region, which can be associated with the unsteady motion of shear layers. For all cases, the locus of peak RMS in each profile seems to collapse well on the dividing streamline. This is consistent with the development of coherent flow motions due to shear layer instabilities, in a fashion similar to Laminar Separation Bubbles (Michelis et al. 2017). Compared to the baseline case, significant increase of velocity fluctuations is observed just downstream of the plasma actuation at  $F^* = 0.25$ . For the case of  $F^* = 1$ , the velocity fluctuation is suppressed considerably as a result of the limited separation region. Chordwise variations of the peak RMS in each velocity profile are further shown in Fig. 10a. At  $F^* \leq 0.25$ , the changing trends of RMS show qualitative similarities. Maximum velocity fluctuations are unexceptionally attained near the separation point

**Fig. 8** **a** Variation of dimensionless backflow area, separation length and lift coefficient with actuation frequency at  $\alpha = 15.5^\circ$ ; **b** Chordwise variation of the boundary layer shape factor ( $H$ ) for increasing actuation frequency; the actuation position is indicated by a black arrow. The separation points determined by zero-velocity line are superimposed as markers



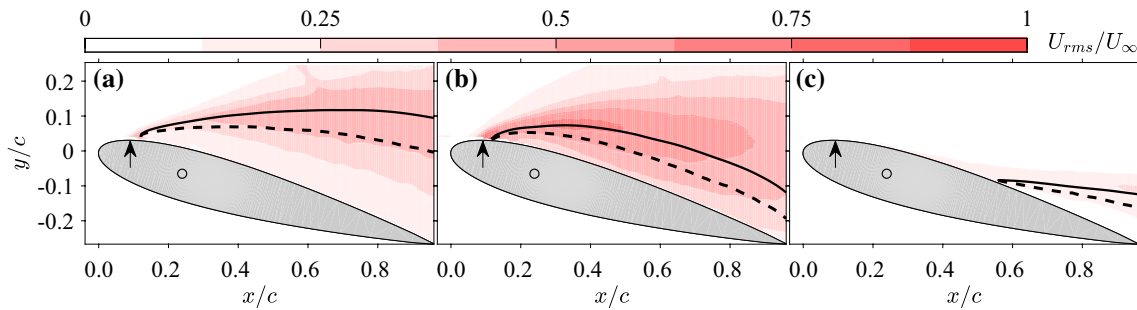
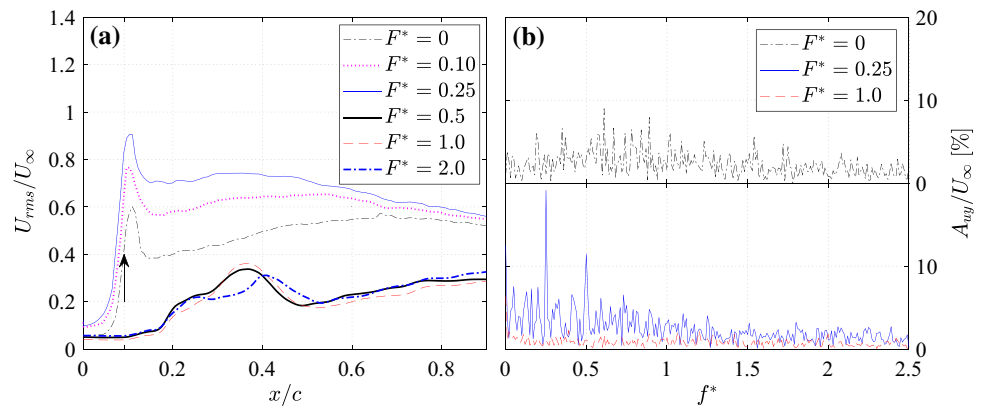


**Fig. 9** Root mean square (RMS) of velocity fluctuations at  $\alpha = 15.5^\circ$ . **a**  $F^* = 0$ ; **b**  $F^* = 0.25$ ; **c**  $F^* = 1.0$

**Fig. 10 a** Chordwise variation of the peak RMS at  $\alpha = 15.5^\circ$  for increasing actuation frequency; **b** frequency spectrum of velocity fluctuations probed on the dividing streamline at  $x/c = 0.4$ . The actuation position is indicated by a black arrow



(approximately  $x = -0.12c$ ) and increase monotonically with actuation frequency. For the cases of  $F^* \geq 0.5$ , actuation frequency has negligible effect on the chordwise variation of RMS, and maximum velocity fluctuations are reached always upstream of the actuation position (approximately  $x = 0.1c$ ). These two distinct regimes in velocity fluctuations suggest the existence of two, respectively, distinct mechanisms of PSJ-based flow control. Further analysis on these two mechanisms is provided in the following sections.

The effect of actuation frequency on velocity fluctuations can also be illustrated in the frequency domain using fast fourier transformation (sample size 2700, frequency resolution 0.6 Hz). Three representative cases are analyzed, where probes are placed on the dividing streamline at  $x = 0.5c$  to sense the fluttering motion of the separated shear layers. The instantaneous velocity in  $y$ -direction ( $u_y$ ) is monitored and the corresponding amplitude spectrum is denoted as  $A_{u_y}$ . As shown in Fig. 10b, the baseline shear layer exhibits several noticeable peaks in the range of  $0.5 \leq f^* \leq 1$  with an amplitude of 5–10% of  $U_\infty$ . When PSJ actuation is applied at  $F^* = 0.25$ , two prominent peaks are created ( $f^* = 0.25$  and  $f^* = 0.5$ ), suggesting that the fluttering motion of the separated shear layer has been modulated accordingly. The mechanisms of this periodical modulation will be introduced later on. For the case of  $F^* = 1.0$ , the separated shear layer shifts downstream and the unsteady motion is largely

suppressed. No dominant frequency components can be picked at  $f^* \leq 2.5$ , possibly due to the long convection distance between actuation and separation.

Based on the signals registered from the discharge and PIV systems, phase-averaged velocity fields at different actuation frequencies can be computed. Figure 11a shows the phase-averaged variation of backflow area. For cases of  $F^* \geq 0.5$  (namely limited trailing edge separation cases), the backflow area remains almost unchanged in one cycle. In contrast, considerable variations of  $A_b^*$  are experienced in cases of  $F^* \leq 0.25$ , which is consistent with the frequency spectrum analysis. For these cases, the backflow area keeps unchanged during the first half time unit after actuation, experiences a sharp drop subsequently and resumes gradually to the undisturbed value. The minimum backflow area is reached at about  $tU_\infty/c = 2$ . In the case of  $F^* = 0.1$ , a plateau is observed at  $T^* \geq 5$ , indicating that the disturbance created by a single pulsed jet has been propagated away from the airfoil after 5 time units. This time scale will be termed as separation reset time ( $T_r$ ) hereinafter.

To reveal the mechanisms of periodic modulations of the separated shear layer at low actuation frequency, several representative phase-averaged flow fields at  $F^* = 0.25$  are shown in Fig. 12. The vorticity ( $\omega_z$ ) is normalised by  $U_\infty$  and half of the maximum airfoil thickness (b). b is used for normalization as the thickness of vorticity layer is

**Fig. 11** **a** Phase-averaged variation of the backflow area with increasing frequency at  $\alpha = 15.5^\circ$ . **b** Zoomed-in view of the backflow area within one actuation period at  $\alpha = 15.5^\circ$  and  $F^* = 0.25$ . The instants shown in Fig. 12 are indicated by triangles

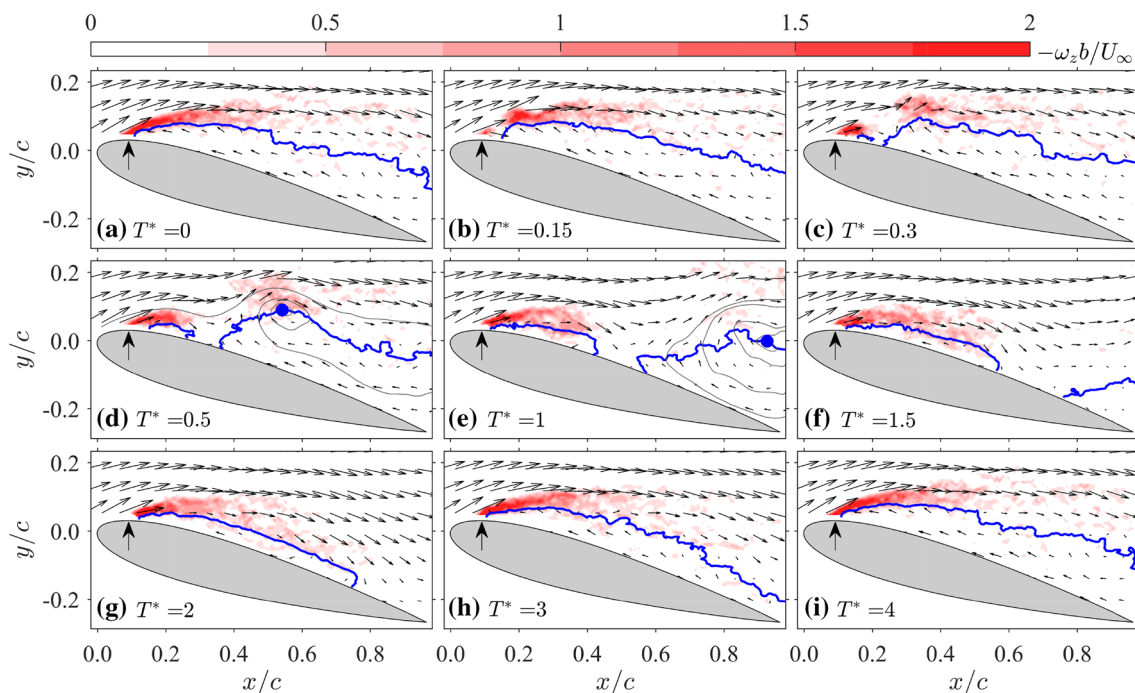
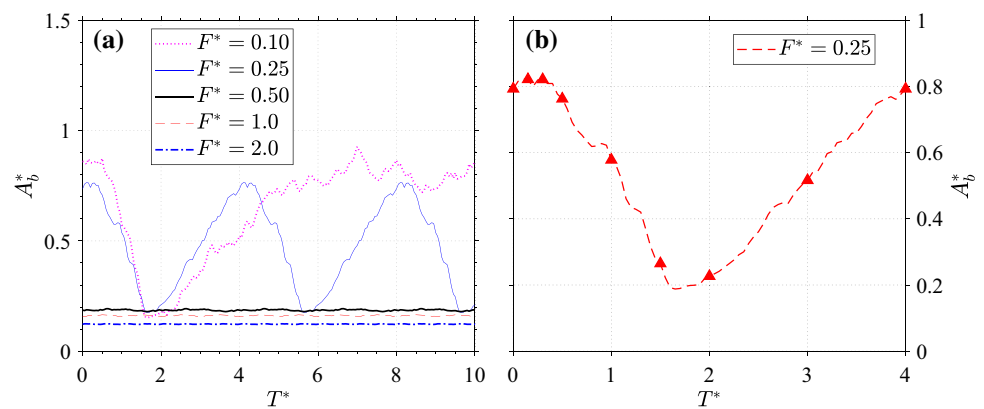


**Fig. 12** Representative phase-averaged flow fields at  $F^* = 0.25$ . The in-plane velocity is presented as thin arrows. The dimensionless spanwise vorticity is superimposed as contours. The thin grey lines and

thick blue lines represent, respectively, streamlines and contour lines of  $U_x = 0$ . Jet positions are indicated by thick black arrows. Vortex centres identified from streamlines are marked by blue dots

close to the airfoil thickness. Additionally, to link the flow field evolution with the variation of integral parameters, a zoomed-in view of the phase-averaged backflow area at  $F^* = 0.25$  in one actuation cycle is plotted in Fig. 11b as a reference. In the undisturbed flow field ( $T^* = 0$ ), vorticity is shed continuously from the leading edge, convecting downstream along the zero-velocity line. After the jet pulse is released, the vorticity shedding is temporarily interrupted ( $T^* = 0.15$ ) and the original vortex sheet is cut into two ( $T^* = 0.3$ ). The downstream vortex sheet gradually rolls into a concentrated vortex ( $T^* = 0.3$  and  $T^* = 0.5$ ) and pushes the original zero-velocity line to the trailing edge during its downstream convection, leading to

a decreasing backflow area ( $0.5 \leq T^* \leq 1.5$ ). At the same time, the upstream vortex sheet gradually convects downstream and remains close to the airfoil surface. Underneath this vortex sheet, a closed separation bubble is formed between  $T^* = 0.5$  and  $T^* = 2$ . As this separation bubble grows, the backflow area increases ( $2 \leq T^* \leq 4$ ), and the vortex sheet is lifted away from the suction surface, resuming towards the undisturbed status. The presence of the closed recirculation region will superimpose a virtual hump on the shape of the original airfoil, thus increasing the effective airfoil camber and the phase-averaged lift. This effect is expected to persist until the bubble bursts at  $T^* = 2.7$  (namely leading-edge separation occurs).



### 4.3 Leading-edge separation control at $\alpha = 22^\circ$ (actuation downstream of separation)

The time-averaged velocity fields at  $\alpha = 22^\circ$  for increasing actuation frequency are shown in Fig. 13. As a result, the separation region can not be reduced effectively by PSJ actuation. This differs significantly from the case shown in Fig. 7b–d, where large-scale leading-edge separation is converted into localized trailing-edge separation. The distinct control effects between  $\alpha = 15.5^\circ$  and  $\alpha = 22^\circ$  can be ascribed to either the relative shift of actuation location (upstream) or the elevated adverse pressure gradient, or both effects simultaneously. The relative importance of these factors cannot be distinguished in the current investigation due to the fixed actuation location. Figure 14a plots the variation

of the normalized backflow area, separation length and lift coefficient with actuation frequency. A non-monotonic change of the backflow area is observed, and the minimum value of  $A_b^*$  (0.65) is reached at  $F^* = 1$ .  $L_s^*$  changes marginally from 0.94 to 0.93 and the separation point remains always upstream of the actuation. Although leading-edge separation is not completely eliminated at  $\alpha = 22^\circ$ , the lift coefficient increase remarkably at  $F^* \leq 1$ , corresponding to the trends pertaining to upstream actuation shown in Fig. 8a. At high actuation frequency ( $F^* = 2$ ),  $C_l$  begins to decrease, leading to an optimal actuation frequency of  $F^* = 1$ .

Chordwise variations of the boundary layer shape factor for increasing frequency are shown in Fig. 14b. For all the tested cases, the shape factor sharply increases at  $x \leq -0.14c$ , and the growth rate is affected marginally by

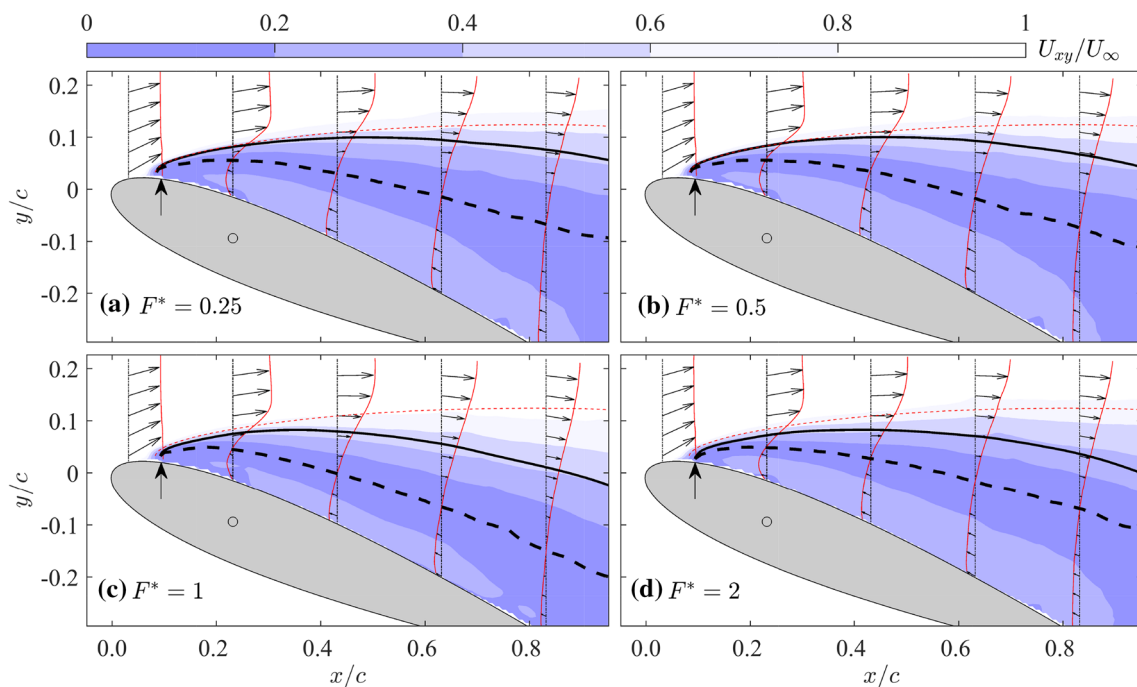
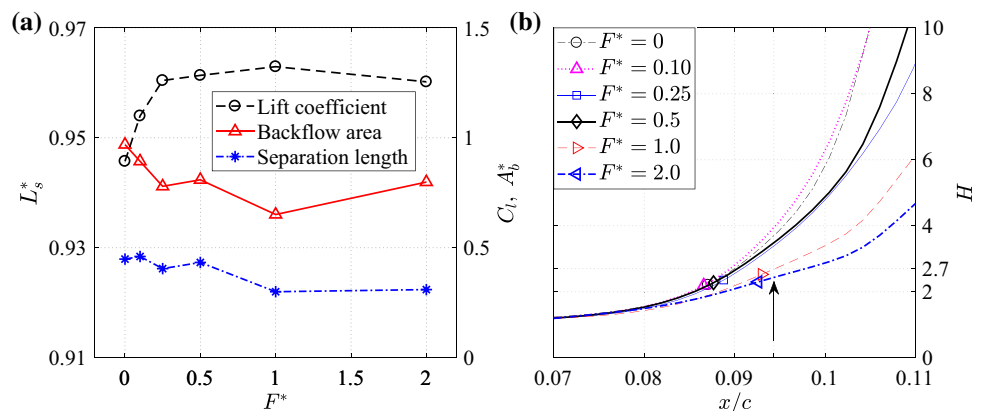


Fig. 13 Time-averaged velocity fields at  $\alpha = 22^\circ$  with PSJ actuation. **a**  $F^* = 0.25$ , **b**  $F^* = 0.5$ , **c**  $F^* = 1$ , **d**  $F^* = 2$ . Identical notation as Fig. 6

Fig. 14 **a** Variation of dimensionless backflow area, separation length and lift coefficient with actuation frequency at  $\alpha = 22^\circ$ ; **b** Chordwise variation of the boundary layer shape factor at  $\alpha = 22^\circ$ ; the actuation position is indicated by a black arrow. The separation points determined by zero-velocity line are superimposed as markers



the plasma actuation. These observations suggest that the incoming boundary layer is not energised sufficiently to withstand the elevated adverse pressure gradient at  $\alpha = 22^\circ$ . Figure 15 displays the RMS of velocity fluctuations in three representative cases. Similar to the flow scenario in Fig. 10, intense velocity fluctuations are generated in the vicinity of the dividing streamlines. Actuated cases exhibit notably higher RMS level than the baseline condition, indicating an enhanced unsteady motion within the separated shear layers due to actuation.

Chordwise evolutions of the peak RMS in wall-normal direction at  $\alpha = 22^\circ$  are shown in Fig. 16a. The baseline case ( $F^* = 0$ ) exhibits similar variation as that at  $\alpha = 15.5^\circ$ . Specifically, maxima of RMS are attained near the separation point (approximately  $x = -0.15c$ ) and a slow increasing trend is experienced downstream of  $x \geq -0.1c$ . With plasma actuation, the RMS located upstream of the jet orifices including the maximum value remains unchanged, whereas the downstream RMS initially increases with actuation frequency and saturates afterwards. This differs noticeably from the upstream actuation case shown in Fig. 10 ( $F^* \leq 0.25$ ) where the entire RMS curve is lifted with increasing frequency. This distinction suggests that PSJ actuation at a location downstream of the separation point is suboptimal in introducing shear layer instabilities and thus enhancing the mixing in the incoming boundary layer. At

$\alpha = 22^\circ$ , PSJs are expelled  $1\%c$  downstream of the separation point, interacting with the reverse flow. As the reverse flow is usually of low velocity, the issued pulsed jets will penetrate through the separated region and leave the upstream boundary layer largely unaffected. This together with an elevated adverse pressure gradient results in a leading-edge detached flow in all the tested cases, and correspondingly low PSJA control authority.

The frequency spectrums probed in the dividing streamlines at  $x = 0.5c$  are displayed in Fig. 16b. Under baseline condition, the separated shear layer exhibits abundant frequency components in the range of  $0.5 \leq f^* \leq 1.7$ . Nevertheless, no single dominant frequency is evident, suggesting a rather broadband receptivity process for the shear layer, near separation. As the baseline spectrum is the result of this broadband amplification of natural disturbances, the range of  $0.5 \leq f^* \leq 1.7$  can be treated as the receptive frequency range of the separated shear layer. This range is wider than the baseline case of  $\alpha = 15.5^\circ$  ( $0.5 \leq f^* \leq 1.0$ ). When plasma actuation is applied within this receptive range ( $F^* = 1.0$ ), only one pronounced peak at the base actuation frequency is created. By contrast, at  $F^* = 0.25$ , several high-order harmonics residing inside the receptive range also appear.

The phase-averaged evolution of the backflow area within one actuation cycle is shown in Fig. 17a. Periodic variations

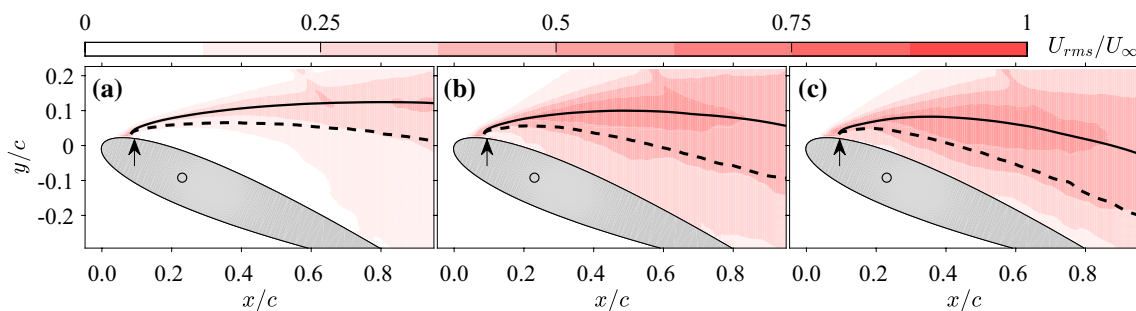
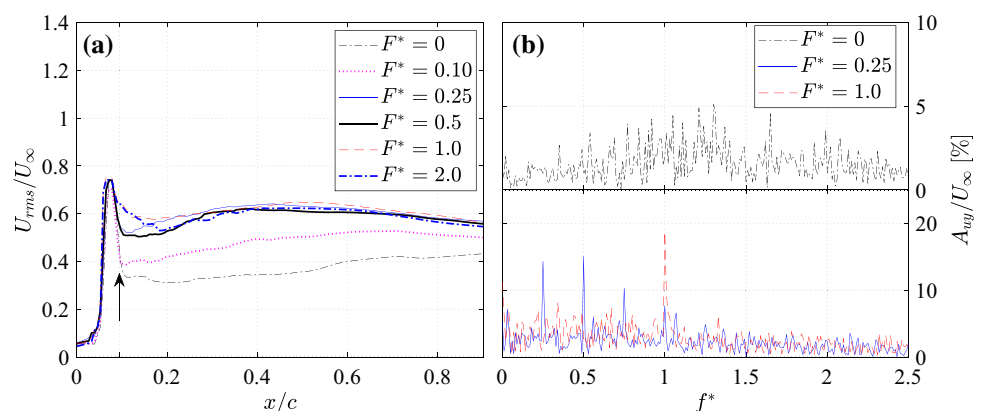
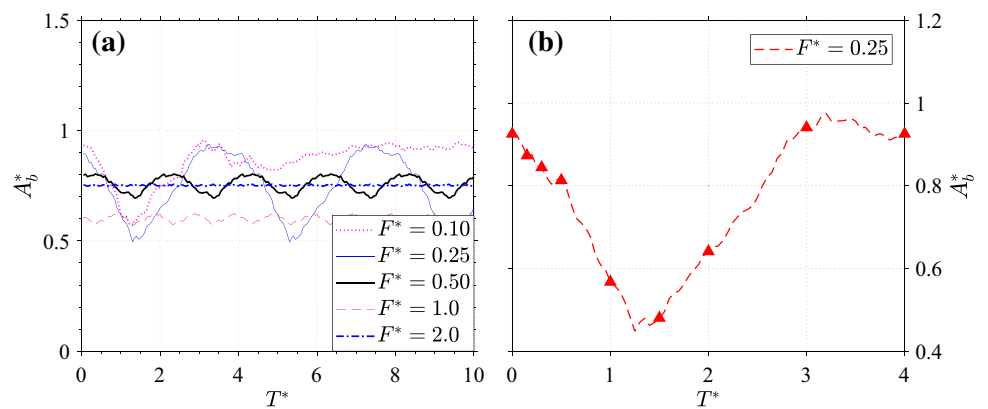


Fig. 15 Root mean square (RMS) of velocity fluctuations at  $\alpha = 22^\circ$ . **a**  $F^* = 0$ ; **b**  $F^* = 0.25$ ; **c**  $F^* = 1.0$

Fig. 16 **a** Chordwise variation of the peak RMS at  $\alpha = 22^\circ$  for increasing frequency; **b** frequency spectrums probed in the dividing streamline at  $x/c = 0.4$ ; the actuation position is indicated by a black arrow



**Fig. 17** **a** Phase-averaged variation of the backflow area with increasing frequency at  $\alpha = 22^\circ$ . **b** Zoomed-in view of the phase-averaged backflow area in one actuation period at  $F^* = 0.25$ ,  $F^* = 0.25$ . The instants shown in Fig. 18 are indicated by triangles



of  $A_b^*$  are observed for cases of  $F^* \leq 1.0$ , pertaining to the dynamic modulation of the separated shear layers by plasma actuation. At  $F^* = 0.1$ , the time response of  $A_b^*$  to a single PSJ pulse is similar to that depicted in Fig. 11, where  $A_b^*$  undergoes a steady decrease shortly after plasma actuation. The minimum value of  $A_b^*$  is attained at about 1.2 time units, slightly earlier than the case shown in Fig. 8 (1.5 time units). Additionally, the time needed for the separated flow to resume after plasma actuation ( $T_r$ ) is approximately 3 time units, which is also shorter than the case of  $\alpha = 15.5^\circ$  (5 time units). The advance of these moments can be attributed to the increasing local velocity associated with wind tunnel blockage, due to the higher angle of attack. The variation of the backflow area at  $F^* = 0.25$  almost duplicates that at  $F^* = 0.1$ , since the corresponding cycle period (4 time units) is long enough to reset the separated flow and the adjacent two jet pulses are essentially independent. Therefore, in the frequency regime of  $F^* \leq 1/T_r$ , increasing the actuation frequency will raise the duty cycle of separation suppression. Consequently, a linear relationship between  $A_b^*$  (as well as  $C_l$ ) and the reduced frequency is expected at  $F^* \leq 0.33$ , which is valid in Fig. 14a. When  $F^*$  exceeds  $1/T_r$ , the adjacent two jet pulses will inevitably interact with each other and the modulation of the separated flow becomes less effective. Consequently, the variation in amplitude of the backflow area decreases with actuation frequency as evidenced by Fig. 17a.

The time evolution of the phase-averaged flow fields at  $F^* = 0.25$  within one actuation cycle is shown in Fig. 18. A zoomed-in view of the corresponding backflow area is plotted in Fig. 17b. Overall, the dynamic response of the separated flow to PSJ actuation at  $\alpha = 22^\circ$  is similar to that at  $\alpha = 15.5^\circ$ . The vortex shedding is also temporally intercepted by the pulsed jet at  $T^* = 0.15$ , and the new-born vortex sheet evolves into a concentrated spanwise vortex which can be well visualized by the streamlines at  $T^* = 1.5$  and  $T^* = 2.0$ . However, unlike the case shown in Fig. 12, the backflow region underneath this spanwise vortex is always connected to the original backflow region after  $T^* = 0.3$ , and

no closed separation bubble is formed. This phenomenon illustrates that the high-momentum fluids transported from the free-stream to the near-wall region are not enough to withstand the severe adverse pressure gradient, ostensibly because the center of this vortex is located too far away from the airfoil surface due to the large angle of attack. Nevertheless, the downwash effect of the spanwise vortex is able to sweep the zero-velocity line towards the suction surface during downstream propagation, leading to a reduced backflow area between  $T^* = 0.5$  and  $T^* = 1.5$ . After  $T^* = 1.5$ , the vortex sheet as well as the suppressed zero-velocity line starts to recover, resulting in an increasing backflow area.

Based on Figs. 12 and 18, the post-stall flow scenario excited by PSJs seems to be dominated by the large-scale vortices shed from the separated shear layer. These vortices convect periodically over the suction surface, increasing the time-averaged lift coefficient at post-stall regime in a similar fashion as that observed in the dynamic stall of pitching airfoils (Corke and Thomas 2015). Specifically, once the pitching angle exceeds the static stall angle, a stall vortex is shed from the leading edge and creates a convective low-pressure core over the suction side, resulting in a lift that is much higher than the static peak lift. This separation control mechanism is consistent with that of SDBDAs driven by high-voltage nanosecond pulses (Little et al. 2012).

The phase-averaged flow fields at  $F^* = 1$  and  $F^* = 2$  are further presented in Figs. 19 and 20 to interpret the formation mechanism of the optimal actuation frequency in Fig. 14 a. At  $F^* = 1$ , two vortices, approximately half a chord apart, can be clearly identified from the streamline patterns throughout the time. As explained earlier, these vortices are created by periodically intercepting the leading-edge vorticity shedding with pulsed jets. The modulation extent of the zero-velocity lines increases with the intensity and size of these spanwise vortices. For the presented case of  $F^* = 1$ , the interaction between adjacent vortices is insignificant due to the sufficient convection distance in one period ( $0.5c$ ). As such, each vortex can grow to considerable size and modulate the backflow area effectively. In the case of  $F^* = 2$ , the vortices are generated every half a time

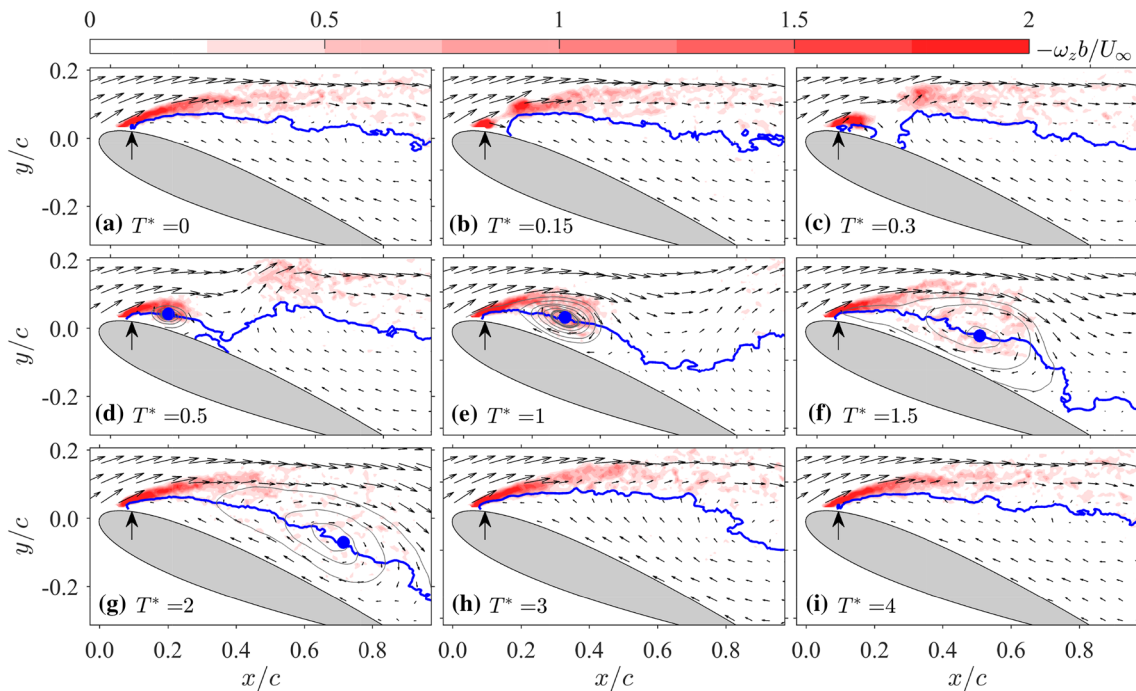


**Fig. 18** Representative phase-averaged flow fields at  $F^* = 0.25$  and  $\alpha = 22^\circ$ ; **a**  $T^* = 0$ , **b**  $T^* = 0.15$ , **c**  $T^* = 0.3$ , **d**  $T^* = 0.5$ , **e**  $T^* = 1$ , **f**  $T^* = 1.5$ , **g**  $T^* = 2$ , **h**  $T^* = 3$ , **i**  $T^* = 4$ . Identical notation as Fig. 12

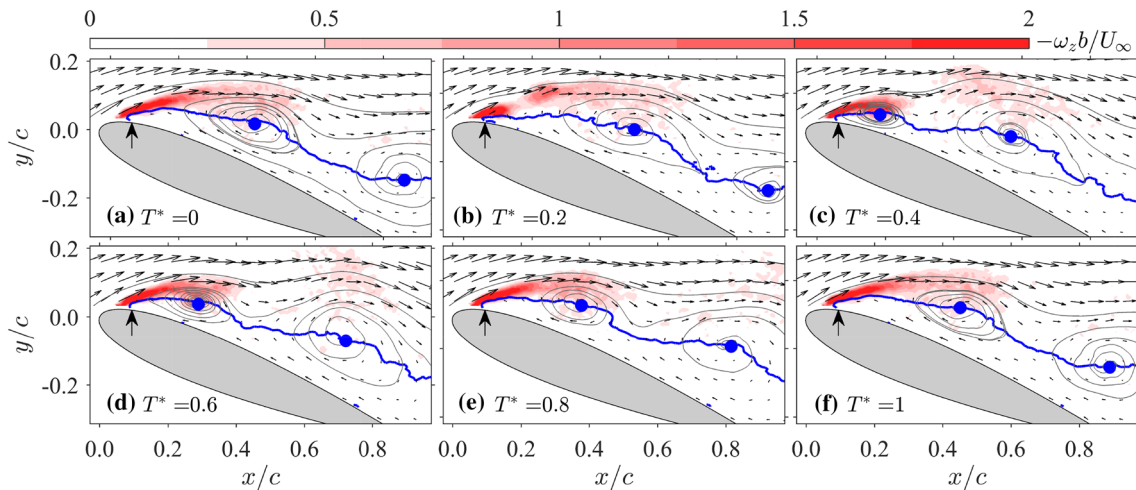


**Fig. 19** Representative phase-averaged flow fields at  $F^* = 1$  and  $\alpha = 22^\circ$ ; **a**  $T^* = 0$ , **b**  $T^* = 0.2$ , **c**  $T^* = 0.4$ , **d**  $T^* = 0.6$ , **e**  $T^* = 0.8$ , **f**  $T^* = 1$ . Identical notation as Fig. 12

unit and the chordwise spacing is reduced to approximately  $0.3c$ . On the one hand, the total vorticity entrained into each vortex (namely circulation) is largely decreased, as a result of this limited growth time. On the other hand, the mutual interaction between adjacent vortices aggravates under the condition of short spacing. Specifically, the generated vortices are rotating in the clockwise direction. The downwash effect of a newborn vortex can be partially counteracted by the upwash effect of the antecedent vortex while propagating downstream, which

leads to an ineffective modulation of the backflow area and a decreasing trend of the lift coefficient after  $F^* \geq 1$  (Fig. 14a).

### 5 Concluding remarks

In the present study, a PSJA array consisting of 26 individual actuators is embedded at 8% chord away from the leading edge of a NACA0015 airfoil model to control the flow



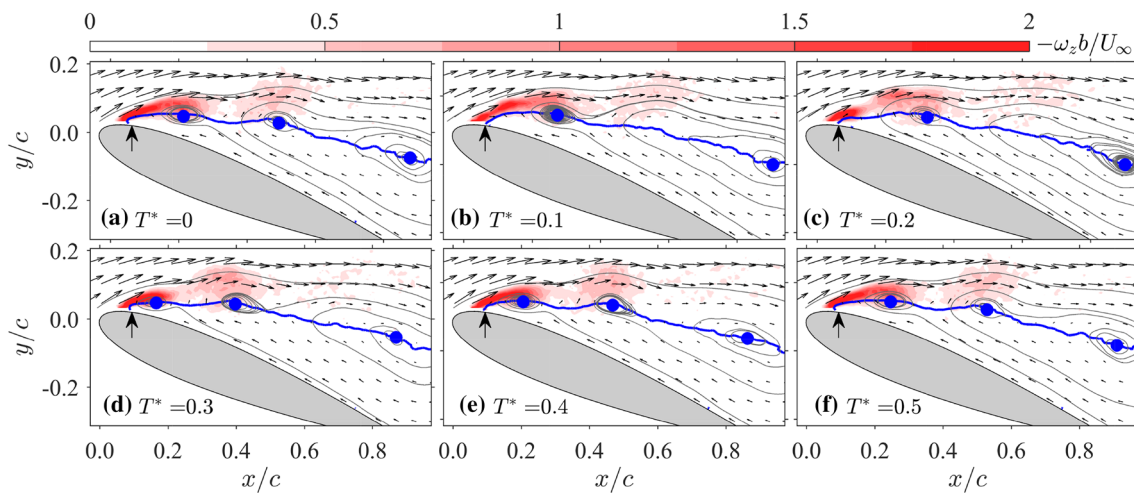


**Fig. 20** Representative phase-averaged flow fields at  $F^* = 2$  and  $\alpha = 22^\circ$ ; **a**  $T^* = 0$ , **b**  $T^* = 0.1$ , **c**  $T^* = 0.2$ , **d**  $T^* = 0.3$ , **e**  $T^* = 0.4$ , **f**  $T^* = 0.5$ . Identical notation as Fig. 12

separation at moderate Reynolds number ( $Re_c = 1.7 \times 10^5$ ,  $U_\infty = 10$  m/s). Balance measurements are performed to evaluate the overall airfoil performance, while high-speed PIV measurements are conducted to reveal the control mechanisms at two critical angles of attack ( $\alpha = 15.5^\circ$  and  $22^\circ$ ), corresponding, respectively, to the incipient and deep stall. In the range of  $0.5 \leq F^* \leq 2$ , the stall angle is postponed from  $15.5^\circ$  to approximately  $22^\circ$ , accompanied by 21% increase in the peak lift coefficient and 40% decrease in the drag coefficient at  $\alpha = 15.5^\circ$ . Hysteresis loops are completely eliminated by PSJ actuation in all cases, while the power saving ratio of PSJAs at  $F^* = 0.5$  and  $\alpha = 15.5^\circ$  is comparable to that of SDBDAs in cylinder flow control by same definition.

At  $\alpha = 15.5^\circ$ , the flow detaches approximately 4%*c* downstream of the jet orifice. When PSJ actuation is applied at  $F^* \geq 0.5$ , the large-scale leading-edge separation under baseline condition is converted into localised trailing-edge separation, similar to the flow scenario observed at  $\alpha = 15^\circ$ . Energizing of the boundary layer resulting from mixing enhancement is responsible for the separation suppression in this frequency range, and the backflow area decreases consistently with increasing frequency. With low-frequency actuation imposed at  $F^* \leq 0.25$ , the separation point still resides near the leading edge, nevertheless the backflow area decreases and the lift coefficient increases linearly with actuation frequency. In these cases, coherent spanwise vortices are generated during the interaction between the array of pulsed jets and the separated shear layer. These vortices transport the high-momentum flow from free stream to the near-wall region and sweep the zero-velocity line periodically

towards the suction surface, leading to a reduction of time-averaged separation area. Additionally, these spanwise vortices will create low-pressure cores on the suction surface which resume the lift.

When  $\alpha$  increases to  $22^\circ$ , the separation point displaces upstream of the jet orifice (1%*c* apart). For PSJ actuation applied between  $F^* = 0.25$  and  $F^* = 2$ , the separation zone retreats downstream marginally as the incoming boundary layer is insufficiently energised. A non-monotonic variation of the lift coefficient and backflow area is observed with increasing frequency, with the optimal actuation frequency located at  $F^* = 1$ . The time evolution of the separated flow at  $F^* \leq 1$  remains similar to the cases of  $F^* \leq 0.25$  and  $\alpha = 15.5^\circ$ , where spanwise vortices are generated consecutively and modulate the separated flow independently. However, at higher actuation frequency ( $F^* = 2$ ), the adjacent spanwise vortices start to interact with each other inevitably due to short streamwise spacing, leading to an ineffective modulation of the separation flow. As a result, the backflow area increases and the lift coefficient declines with increasing frequency after  $F^* = 2$ .

To sum up, the ability of PSJAs to suppress the airfoil flow separation at moderate Reynolds number is experimentally verified. In future steps, the discharge circuit should be upgraded to be able to feed the actuators at high frequency ( $O(1$  kHz)), and the control authority of the actuators at higher freestream velocity and more practical Reynolds number (i.e.,  $O(1 \times 10^6)$ ) should be explored.

**Open Access** This article is distributed under the terms of the Creative Commons Attribution 4.0 International License (<http://creativecommons.org/licenses/by/4.0/>), which permits unrestricted use, distribution, and reproduction in any medium, provided you give appropriate credit to the original author(s) and the source, provide a link to the Creative Commons license, and indicate if changes were made.



## References

- Amitay M, Smith DR, Kibens V, Parekh DE, Glezer A (2001) Aerodynamic flow control over an unconventional airfoil using synthetic jet actuators. *AIAA J* 39(3):361–370. <https://doi.org/10.2514/2.1323>
- Anderson KV, Knight DD (2012) Plasma jet for flight control. *AIAA J* 50(9):1855–1872. <https://doi.org/10.2514/1.J051309>
- Belinger A, Naudé N, Cambonne JP, Caruana D (2014) Plasma synthetic jet actuator: electrical and optical analysis of the discharge. *J Phys D Appl Phys* 47(34):345202. <https://doi.org/10.1088/0022-3727/47/34/345202>
- Benard N, Moreau E (2014) Electrical and mechanical characteristics of surface AC dielectric barrier discharge plasma actuators applied to airflow control. *Exp Fluids* 55(11):1846. <https://doi.org/10.1007/s00348-014-1846-x>
- Benard N, Cattafesta LN, Moreau E, Griffin J, Bonnet J (2011) On the benefits of hysteresis effects for closed-loop separation control using plasma actuation. *Phys Fluids* 23(8):083601. <https://doi.org/10.1063/1.3614482>
- Caruana D, Rogier F, Dufour G, Gleyzes C (2013) The plasma synthetic jet actuator, physics, modeling and flow control application on separation. *J AerospaceLab* 6:1–13
- Cattafesta LN, Sheplak M (2011) Actuators for active flow control. *Ann Rev Fluid Mech* 43:247–272. <https://doi.org/10.1146/annurev-fluid-122109-160634>
- Chiatto M, de Luca L (2017) Numerical and experimental frequency response of plasma synthetic jet actuators. In: 55th AIAA aerospace sciences meeting. AIAA 2017-1884, pp 1–16. <https://doi.org/10.2514/6.2017-1884>
- Choi H, Jeon WP, Kim J (2008) Control of flow over a bluff body. *Ann Rev Fluid Mech* 40:113–139
- Compton D, Johnston J (1992) Streamwise vortex production by pitched and skewed jets in a turbulent boundary layer. *AIAA J* 30(3):640–647. <https://doi.org/10.2514/6.1991-38>
- Corke TC, Thomas FO (2015) Dynamic stall in pitching airfoils: aerodynamic damping and compressibility effects. *Ann Rev Fluid Mech* 47:479–505. <https://doi.org/10.1146/annurev-fluid-010814-013632>
- Corke TC, Enloe CL, Wilkinson SP (2010) Dielectric barrier discharge plasma actuators for flow control. *Ann Rev Fluid Mech* 42:505–529. <https://doi.org/10.1146/annurev-fluid-121110-8-145550>
- Correale G, Michelis T, Ragni D, Kotsonis M, Scarano F (2014) Nanosecond-pulsed plasma actuation in quiescent air and laminar boundary layer. *J Phys D Appl Phys* 47(10):105201. <https://doi.org/10.1088/0022-3727/47/10/105201>
- Gad-el Hak M, Pollard A, Bonnet JP (2003) Flow control: fundamentals and practices, vol 53. Springer Science & Business Media, Berlin
- Giepmans RHM, Kotsonis M (2011) On the mechanical efficiency of dielectric barrier discharge plasma actuators. *Appl Phys Lett* 98(22):1054:1–3. <https://doi.org/10.1063/1.3597652>
- Glezer A, Amitay M, Honohan AM (2005) Aspects of low- and high-frequency actuation for aerodynamic flow control. *AIAA J* 43(7):1501–1511. <https://doi.org/10.2514/1.7411>
- Greenblatt D, Wygnanski IJ (2000) The control of flow separation by periodic excitation. *Prog Aerosp Sci* 36:487–545. <https://doi.org/10.2514/6.2004-2505>
- Greene BR, Clemens NT, Magari P, Micka D (2015) Control of mean separation in shock boundary layer interaction using pulsed plasma jets. *Shock Waves* 25(5):495–505. <https://doi.org/10.1007/s00193-014-0524-5>
- Grossman KR, Cybyk BZ, VanWie DM (2003) Sparkjet actuators for flow control. In: 41st Aerospace sciences meeting and exhibit 2003-57, pp 1–9. <https://doi.org/10.1038/NMAT2404>. arXiv:1206.5023
- Haack SJ, Taylor T, Emshoff J, Cybyk B (2010) Development of an analytical sparkjet model. In: 5th Flow control conference. AIAA 2010-4979, pp 1–10. <https://doi.org/10.2514/6.2010-4979>
- Jukes TN, Choi KS (2009) Long lasting modifications to vortex shedding using a short plasma excitation. *Phys Rev Lett* 102(25):254,501. <https://doi.org/10.1103/PhysRevLett.102.254501>
- Lardeau S, Leschziner M (2011) The interaction of round synthetic jets with a turbulent boundary layer separating from a rounded ramp. *J Fluid Mech* 683:172–211
- Little J, Takashima K, Nishihara M, Adamovich I, Samimy M (2012) Separation control with nanosecond-pulse-driven dielectric barrier discharge plasma actuators. *AIAA J* 50(2):350–365. <https://doi.org/10.2514/1.J051114>
- Marchman J III, Sumantran V, Schaefer C (1987) Acoustic and turbulence influences on stall hysteresis. *AIAA J* 25(1):50–51
- Maskell E (1963) A theory of the blockage effects on bluff bodies and stalled wings in a closed wind tunnel. Tech. rep., Aeronautical Research Council London (United Kingdom)
- Michelis T, Yarusevych S, Kotsonis M (2017) Response of a laminar separation bubble to impulsive forcing. *J Fluid Mech* 820:633–666
- Mittal R, Rampunggoon P (2002) On the virtual aeroshaping effect of synthetic jets. *Phys Fluids* 14(4):1533–1536. <https://doi.org/10.1063/1.1453470>
- Narayanaswamy V, Raja LL, Clemens NT (2010) Characterization of a high-frequency pulsed-plasma jet actuator for supersonic flow control. *AIAA J* 48(2):297–305. <https://doi.org/10.2514/1.41352>
- Narayanaswamy V, Raja LL, Clemens NT (2012) Control of unsteadiness of a shock wave/turbulent boundary layer interaction by using a pulsed-plasma-jet actuator. *Phys Fluids* 24(7):076,101. <https://doi.org/10.1063/1.4731292>
- Post ML, Corke TC (2004a) Separation control on high angle of attack airfoil using plasma actuators. *AIAA J* 42(11):2177–2184. <https://doi.org/10.2514/1.2929>
- Post ML, Corke TC (2004b) Separation control using plasma actuators-stationary & oscillating airfoils. In: 42nd AIAA aerospace sciences meeting and exhibit, AIAA 2004-0841, pp 1–12
- Postl D, Balzer W, Fasel HF (2011) Control of laminar separation using pulsed vortex generator jets: direct numerical simulations. *J Fluid Mech* 676:81–109. <https://doi.org/10.1017/jfm.2011.34>
- Roupasov DV, Nikipelov AA, Nudnova MM, Starikovskii AY (2009) Flow separation control by plasma actuator with nanosecond pulsed-periodic discharge. *AIAA J* 47(1):168–185. <https://doi.org/10.2514/1.38113>
- Schlichting H, Gersten K (2017) Boundary-layer theory. Springer, Berlin. <https://doi.org/10.1007/978-3-662-52919-5>
- Sciacchitano A, Wieneke B (2016) PIV uncertainty propagation. *Meas Sci Technol* 27(8):084006. <https://doi.org/10.1088/0957-0233/27/8/084006>
- Seifert A, Greenblatt D, Wygnanski IJ (2004) Active separation control: an overview of Reynolds and Mach numbers effects. *Aerosp Sci Technol* 8:569–582. <https://doi.org/10.1016/j.ast.2004.06.007>
- Simpson R (1989) Turbulent boundary-layer separation. *Ann Rev Fluid Mech* 21:205–234. <https://doi.org/10.1146/annurev.fluid.21.1.205>
- Smy P, Clements R, Dale J, Simeoni D, Topham D (1983) Efficiency and erosion characteristics of plasma jet igniters. *J Phys D Appl Phys* 16(5):783
- Timmer W (2008) Two-dimensional low-Reynolds number wind tunnel results for airfoil naca 0018. *Wind Eng* 32(6):525–537
- Yarusevych S, Sullivan PE, Kawall JG (2009) On vortex shedding from an airfoil in low-Reynolds-number flows. *J Fluid Mech* 632:245–271. <https://doi.org/10.1017/S0022112009007058>

- Zhang Z, Wu Y, Jia M, Song H, Sun Z, Zong H, Li Y (2017a) The multichannel discharge plasma synthetic jet actuator. *Sens Actuators A Phys* 253:112–117. <https://doi.org/10.1016/j.sna.2016.11.011>
- Zhang Z, Wu Y, Jia M, Song Z, Sun ZZ, Li Y (2017b) Modeling and optimization of the multichannel spark discharge. *Chin Phys B* 26(6):065204. <https://doi.org/10.1088/1674-1056/26/6/065204>
- Zong H, Kotsonis M (2016a) Characterisation of plasma synthetic jet actuators in quiescent flow. *J Phys D Appl Phys* 49(33):335202. <https://doi.org/10.1088/0022-3727/49/33/335202>
- Zong H, Kotsonis M (2016b) Electro-mechanical efficiency of plasma synthetic jet actuator driven by capacitive discharge. *J Phys D Appl Phys* 49(45):455201. <https://doi.org/10.1088/0022-3727/49/45/455201>
- Zong H, Kotsonis M (2017a) Experimental investigation on frequency characteristics of plasma synthetic jets. *Phys Fluids* 29(11):115107
- Zong H, Kotsonis M (2017b) Interaction between plasma synthetic jet and subsonic turbulent boundary layer. *Phys Fluids* 29(4):045104. <https://doi.org/10.1063/1.4979527>
- Zong H, Kotsonis M (2017c) Realisation of plasma synthetic jet array with a novel sequential discharge. *Sens Actuators A Phys* 266:314–317
- Zong H, Kotsonis M (2018) Formation, evolution and scaling of plasma synthetic jets. *J Fluid Mech* 837:147–181
- Zong H, Wu Y, Li Y, Song H, Zhang Z, Jia M (2015) Analytic model and frequency characteristics of plasma synthetic jet actuator. *Phys Fluids* 27(2):027105. <https://doi.org/10.1063/1.4908071>
- Zong H, Wu Y, Jia M, Song H, Liang H, Li Y, Zhang Z (2016) Influence of geometrical parameters on performance of plasma synthetic jet actuator. *J Phys D Appl Phys* 49(2):025504. <https://doi.org/10.1088/0022-3727/49/2/025504>

**Publisher's Note** Springer Nature remains neutral with regard to jurisdictional claims in published maps and institutional affiliations.